The Thesis committee for Samuel Thomas Harrold

Certifies that this is the approved version of the following thesis:

Calculating the structure of protoplanetary disks within the first few AU using Pisco

APPROVED BY

SUPERVISING COMMITTEE:

Supervisor: ________________________________

John Lacy

____

Dan Jaffe

Calculating the structure of protoplanetary disks within the first few AU using Pisco

by

Samuel Thomas Harrold, B.S.; B.A.

Thesis

Presented to the Faculty of the Graduate School

of The University of Texas at Austin

in Partial Fulfillment

of the Requirements

for the Degree of

Master of Arts

The University of Texas at Austin

December 2011

Calculating the structure of protoplanetary disks within the first few AU using Pisco

by

Samuel Thomas Harrold, M.A.
The University of Texas at Austin, 2011
SUPERVISOR: John Lacy

The calculation of the physical conditions near the inner rim of a protoplanetary disk using the new computational model Pisco is described. Diagnostic plots illustrate solutions for disk structure, radiation field, chemical composition, and heating and cooling of the disk in a steady-state approximation for both disks with unsettled dust and with settled dust. Disks with unsettled dust are found to have hotter gas temperatures above the disk photosphere and a more pronounced temperature inversion at the disk photosphere. Recommendations are made for the development of Pisco. Pisco has the potential to explore what observed molecular emission can imply about disk structure.

Contents

Chapter 1

Introduction

A protoplanetary disk is a disk of gas and dust surrounding a newborn star (Kenyon & Hartmann, 1987) and is the remnant of star formation (Kenyon & Hartmann, 1995). Over the course of 1-2 million years, the gas and dust will stratify as the dust settles through the gas to the midplane and coagulates to form planetesimals (Haisch et al., 2001). Settling the dust through a disk changes the intensity and wavelength of radiation incident at a given coordinate location within disk. The subsequent heating and cooling of the disk will likewise change and thereby alter the physical conditions within the disk. Understanding the physical conditions within protoplanetary disks is key to understanding planet formation.

Spectroscopic observations of protoplanetary disks provide constraints on the total emission from cooling mechanisms that regulate the temperature-dependent physical conditions within the disk. Modern telescopes are currently unable to resolve the inner few AU of a protoplanetary disk, yet it is from this region that much of the observed emission originates (Dullemond & Monnier, 2010). To bridge the gap between observational constraints and theories of disk structure, computational models calculate the disk profile, temperature, density, chemical composition, and radiation field using the physics governing disk structure such that the solved physical quantities are consistent with observations.

In this thesis, a new 2+1D computational model for protoplanetary disks called Pisco is used to iteratively calculate the physical conditions within a sample protoplanetary disk. The comparison of physical conditions for a typical disk with unsettled dust and with settled dust is discussed in the following chapters. Compared to contemporary models (Dullemond et al., 2007; Woitke et al., 2009), the focus of Pisco is to model the inner disk ($\lesssim 5\,\mathrm{AU}$) with high resolution and in steady state as a snapshot of the disk in the course of its evolution. The underlying assumption is that the physical processes modeled come to near equilibrium on a time scale less than that of the dust and disk evolution, c.f. Williams & Cieza (2011); Armitage (2011).

Pisco performs fully 3D ray tracing in calculating radiative transfer, and all other calculations of physical conditions are 2D and assumed to be symmetric about the disk midplane and about the disk's rotational axis. Physical conditions for the model disk are computed iteratively until convergence. As an initial guess, a semi-analytic model in the manner of Chiang & Goldreich (1997) provides a first estimate of gas temperature, dust temperature, pressure, and density for every cell of the computational model. 3D ray tracing over wavelengths spanning from ~0.1 to just short of 1000 μm is performed to calculate the mean intensity at each cell. New temperatures for the gas and dust are calculated by balancing the effects of dust heating by radiative absorption; dust cooling by radiative emission; gas heating by the photoelectric effect, X-ray absorption, and viscosity; gas cooling by atomic and molecular emission lines; and coupling by gas-dust collisions. New gas pressures and densities are calculated for each cell assuming hydrostatic equilibrium. With a new density profile and modified disk shape, the radiation field is then recalculated. Iterations cease once the gas and dust temperatures have sufficiently converged. Pisco is currently under development and benchmark testing, e.g. Pinte et al. (2009). A detailed description of the mechanics of Pisco is in preparation.

The models described within this thesis are those of two 2 Myr-old Class II classical-type (actively accreting) T-Tauri stars with protoplanetary disks (c.f. Hartmann et al., 1998). One disk is modeled with unsettled dust, and the other disk is modeled with settled dust. The specific disk parameters are given in Table 1.1. Differences in the solutions for physical conditions and processes between a disk with settled dust and a disk with unsettled dust are compared in the following chapters: Chapter 2 compares differences in physical structure; Chapter 3 compares differ-

Table 1.1. Model parameters

Stellar parameters:	$M_\star$	$R_\star$	$L_\star$	$T_{\rm eff}$	$\dot{M}_\star$	$L_{\rm X\text{-}ray}$
Disk parameters:	$M_{\rm disk}$	gas/dust [a]	$R_{\rm inner}$ [b]	$\Sigma_{0,\,0.2\,\rm AU}$ [c]	$a_{\rm max}$ [d]	
	$0.8\,M_\odot$	$2.0\,R_\odot$	$1.0\,L_\odot$	4000 K	$10^{-8}\,M_\odot\,\rm yr^{-1}$	$10^{-4}\,M_\odot$
	$10^{-2}\,M_\odot$	100	0.09 AU	$500\,\rm g\,cm^{-2}$	$1\,\mu$m	

[a] Total disk gas mass / total disk dust mass

[b] Calculated radius of disk inner rim from dust sublimation.

[c] Σ_0 = disk surface density

[d] $a_{\rm max}$ = max grain diameter and $a_{\rm max} \propto a^{-3.5}$ (c.f. Weingartner & Draine, 2001)

ences in radiation field; Chapter 4 compares differences in chemical abundances; Chapter 5 compares differences in disk heating; and Chapter 6 compares differences in disk cooling with the addition of methods for calculating cooling via emission by atoms and ions. Chapter 7 concludes with suggestions for future code development.

Chapter 2

Disk structure

The physical structure of a protoplanetary disk and the differences between the profiles of an unsettled disk and a settled disk are best conveyed graphically. Figure 2.1 shows the cross-section of a protoplanetary disk both without and with dust settling in a Cartesian scale, and Figure 2.2 shows a close-up of the inner rim of the disk where dust has sublimated. Contours are plotted to show the line-of-sight optical depth in V-band from the central star into the disk to show the disk's profile as determined from the absorption of visible starlight. For heights $\lesssim 0.015\,\mathrm{AU}$ above the midplane, the magnitude of the optical depth gradient across the inner rim has been artificially reduced to facilitate calculating radiative transfer.

To model the structure of the inner disk in detail, Pisco uses nested grids of cells spaced logarithmically in cylindrical radius by base 2. The cells within each grid are spaced linearly in cylindrical radius. For example, all grids have n radial cells

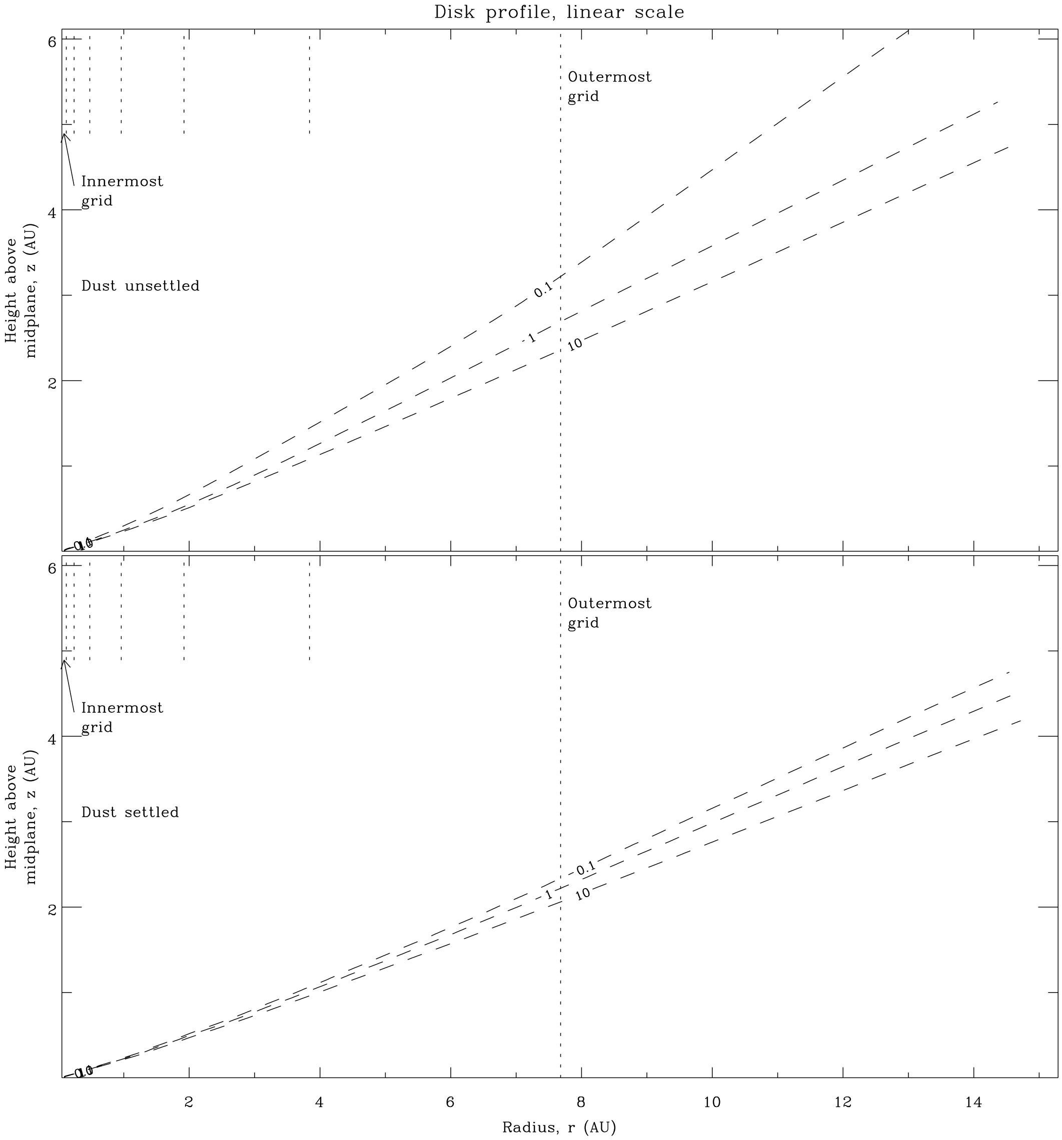

Figure 2.1 The top and bottom plots are cross-sections of a disk without dust settling and with dust settling, respectively. The entire modeled disk is plotted with dashed contours of the line-of-sight optical depth in V-band for rays traced from the star into the disk. The contours correspond to $\tau_V = 0.1, 1, 10$. For perspective, the vertical and radial axes are set to the same distance scale, and the coordinate origin is coincident with the location of the central star. At a radius of about 10 AU for a given line-of-sight optical depth to the star τ_V, dust settling reduces the corresponding scale by ∼15-20%.

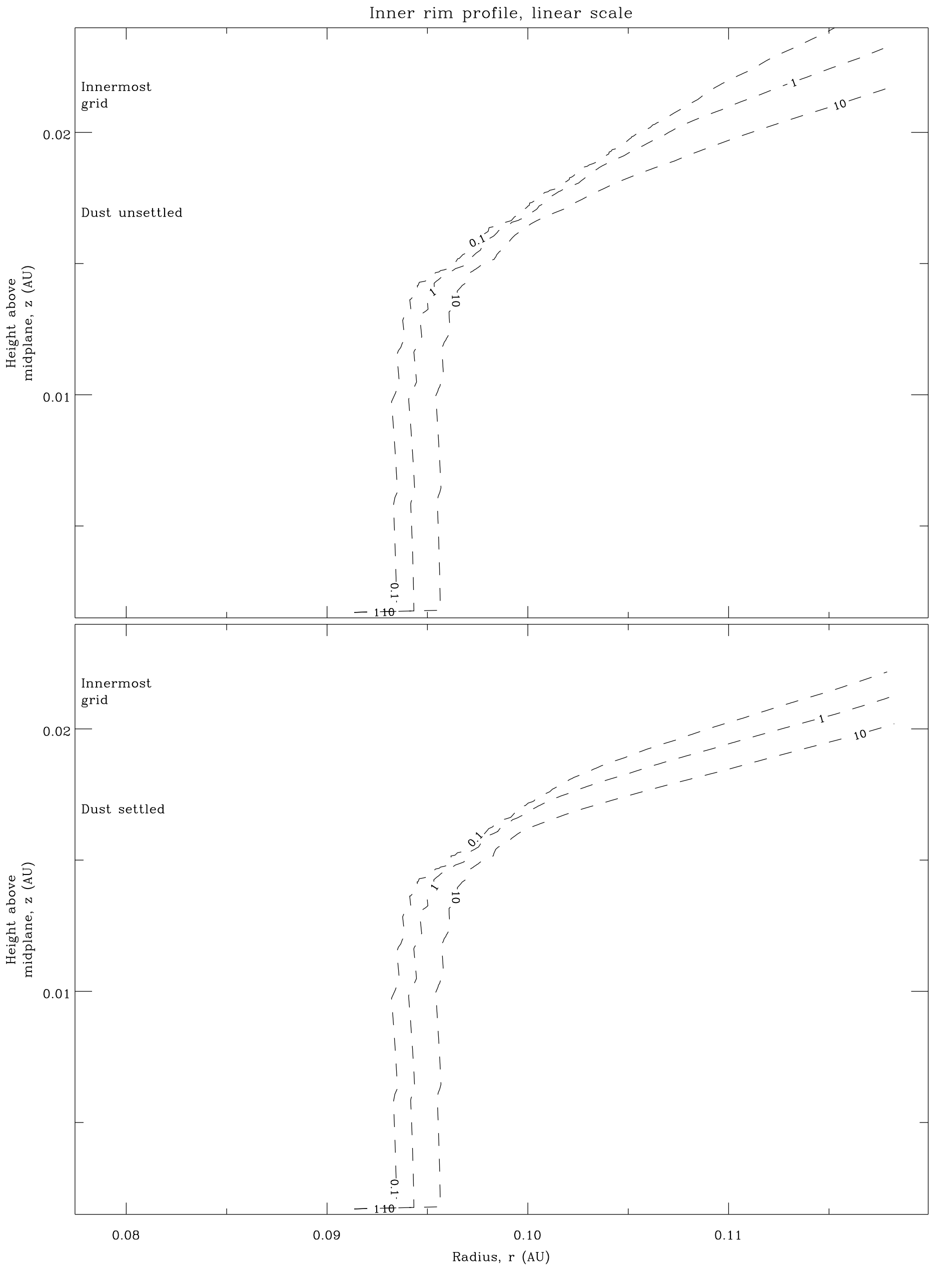

Figure 2.2 The disk inner rim within the innermost grid is plotted for an unsettled disk and a settled disk. The dashed contours are stellar line-of-sight optical depth, and the coordinates are square $r-z$ as in Figure 2.1.

and the innermost grid may span from a radius r to $2r$ with each cell representing a radial distance $(2r - r)/n$. The next grid moving away from the star then spans from $2r$ to $4r$ with each cell representing $(4r - 2r)/n$.

In Figure 2.1 and all subsequent plots, the approximate locations of the radial divisions between the 8 logarithmically-spaced computational grids are marked at the top of each plot as vertical dotted lines with the innermost and outermost grids labeled. Because the calculation abruptly ends at the outer edge of the outermost grid, results within the outermost grid suffer from inconsistent boundary conditions. The vertical dotted line at ∼7.7 AU is extended to the midplane to mark the inner boundary of the outermost grid for all heights above the midplane. To view the modeled protoplanetary disk in its entirety, Figure 2.3 and all subsequent plots of the disk are mapped to rectilinear $\log_2(r - z/r)$ coordinates.

As evident in Figure 2.3, for a fixed value of line-of-sight optical depth to the star at a fixed cylindrical radius, dust settling by Pisco effectively reduces the corresponding height above the midplane. For example, at a radial distance of 10 AU from the central star, a stellar line-of-sight optical depth of unity occurs at a height of ∼3.5 AU above the midplane for the modeled disk with unsettled dust and at a height of ∼3 AU for a settled disk, which is a reduction in height of ∼15%. Dust settling also reduces the flaring of the disk photosphere, but both unsettled and settled disks are flared as calculated here. Contours with a positive slope in z/r as

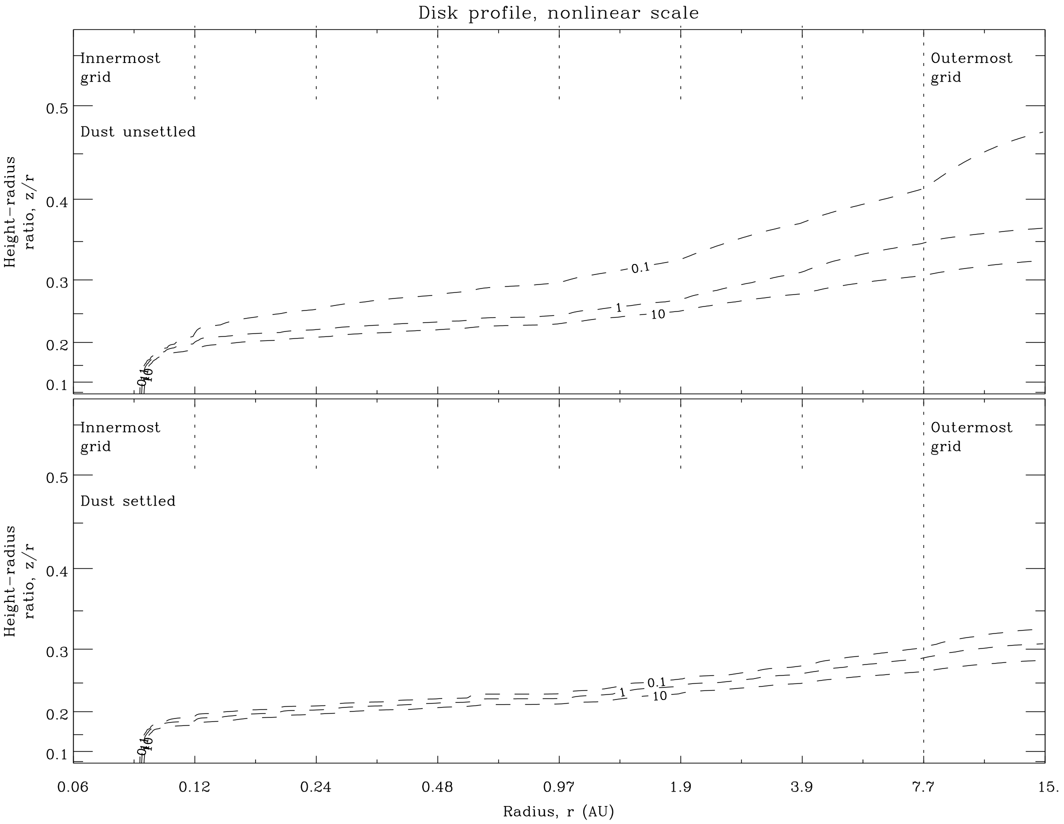

Figure 2.3 The entire modeled disk is plotted for an unsettled disk and a settled disk with dashed contours of stellar line-of-sight optical depth as in Figure 2.1 but in rectilinear $\log_2 r$–z/r coordinates, where r is the radius in cylindrical coordinates.

a function of r indicate flaring of the disk photosphere. This preliminary work is consistent with Dullemond & Dominik (2004).

The physical conditions of the protoplanetary disk are highly dependent on the disk structure. Because gas comprises over 99% of the disk mass for these models, the physical conditions of the gas can characterize those of the disk. Figure 2.4 plots the gas temperature for disks with unsettled and settled dust. The abrupt boundaries between temperatures above the disk in Figure 2.4 are an artifact of different calculations being performed for different local conditions. These boundaries are evident in the plots of all quantities dependent on gas temperature. Going from the upper left corner of Figure 2.4 to the lower right corner, two abrupt boundaries are crossed:

1. The gas temperature is not calculated for gas particle number densities $n_{\mathrm{gas}} \lesssim 10^{-2}\,\mathrm{cm}^{-3}$, Figure 2.5.
2. Where the dust has sublimated, the local gas temperature is assumed to be that of a blackbody, $\propto r^{-1/2}$ (r as spherical radius).

Gas heating and cooling processes are only calculated where dust is presumed to exist. The disk photosphere as described in this thesis is where the line-of-sight optical depth from the star into the disk in V-band, τ_V, is unity. The disk photosphere occurs where both gas and dust exist, which is beneath both calculation

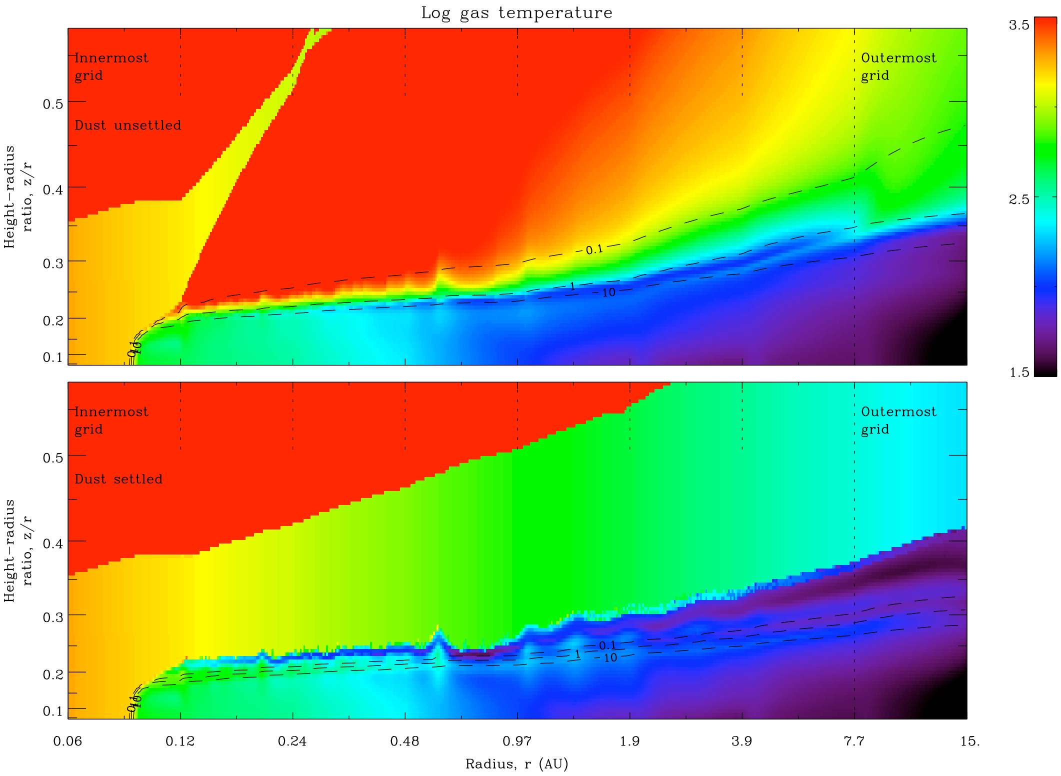

Figure 2.4 The $\log_{10}$ gas temperature (K) for an unsettled disk and a settled disk is plotted as in Figure 2.3. A disk with settled dust has an enhanced temperature inversion at the disk photosphere than a disk with unsettled dust and cooler temperature above the disk photosphere.

boundaries.

From Figure 2.4, the temperature inversion at the disk photosphere first predicted by Chiang & Goldreich (1997) is much stronger in disks with settled dust compared to those with unsettled dust. The gas temperature above the disk photosphere is also hotter when dust is unsettled compared to when it is settled. This is due to increased photoelectric heating (Chapter 5) and implies that an unsettled disk must have enhanced cooling above the disk photosphere (Chapter 6). The enhanced

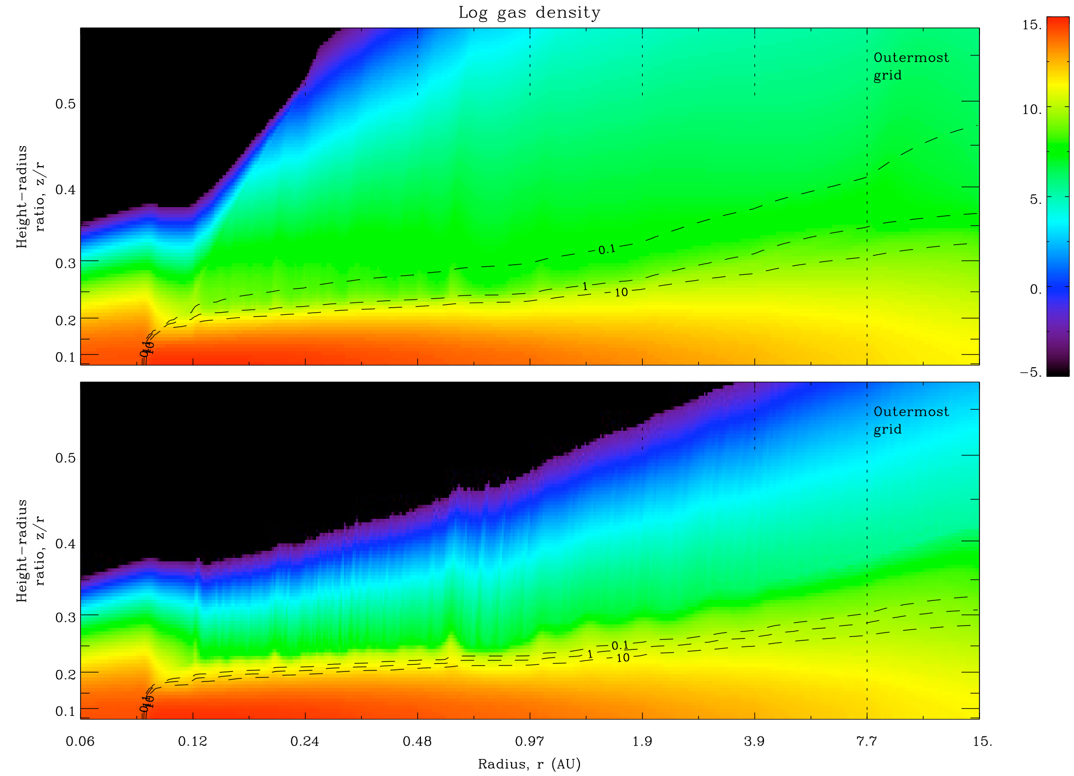

Figure 2.5 The $\log_{10}$ gas particle number density (cm^{-3}) for an unsettled disk and a settled disk is plotted as in Figure 2.4. The jagged structure of the disk surface is the result of discrepancies in radiative transfer across grid divisions.

temperature inversion and higher gas temperature above the disk photosphere are consistent with Kamp & Dullemond (2004). However, the temperature above the photosphere of settled disks is also underestimated due to excessive cooling by CO and H_2O as a result of high abundance assumptions (Chapter 4).

Pisco's calculations of disk temperature and density result in a jagged disk surface structure, Figure 2.5. Discrepancies in the calculation of radiative transfer across grid boundaries amplify heating processes and thus the temperature at those grid boundaries (Chapters 3 and 5). With lower density gas at the grid boundaries, the vertical integration of hydrostatic equilibrium propagates a jagged structure through the disk until terminated at the gas temperature calculation boundary. Iterations of radiative transfer and dust heating and cooling can radially distribute jagged structures across the disk surface. The calculated gas temperature is also pixelated by individual cells along the surface of the settled disk due to instabilities in the cooling calculation (Chapter 6), and this artifact is evident for all quantities dependent on gas temperature.

Atomic and molecular abundances as a function of location within the disk can be parameterized in terms of a gas column density in a given direction, usually in the direction of the star or in the vertical direction out of the disk. This parameterization of abundances is justified because of the dependence of abundances on the local radiation field and because it is necessary to incorporate abundance calculations from other codes, such as those from Glassgold et al. (2004). The abundances used for these disk models are parameterized by the gas column density in the direction of least optical depth, or escape-path column density as described in this thesis. This approximation is inaccurate (Chapter 4).

The escape-path column density, Figure 2.6 is approximated as half the harmonic mean of the column densities in the radial (spherical coordinates) and vertical directions, $N_{\mathrm{esc}} = 1/(1/N_\rho + 1/N_z)$. Beneath the disk surface, $N_\rho \gg N_z$, and thus $N_{\mathrm{esc}} \approx N_z$ as desired. However, $N_{\mathrm{esc}} < N_\rho, N_z$ for all column density values, and it is recommended that N_{esc} be redefined as the harmonic mean of N_ρ and N_z, instead of half the harmonic mean.

Because the gas temperature characterizes that of the disk, the gas-dust temperature coupling indicates the extent that the heating and cooling processes of the dust or gas dominate the temperature regulation of the disk, Figure 2.7. The ratio of the gas-dust temperature difference to gas-dust energy flow, $(T_{\mathrm{g}} - T_{\mathrm{d}})/\Gamma_{\mathrm{g-d}}$, is a measure of the coupling between the gas and dust temperatures and is adapted from Tielens (2005, § 3.5). $T_{\mathrm{g(d)}}$ is the temperature of the gas (dust) in Kelvin, and $\Gamma_{\mathrm{g-d}}$ is the kinetic energy transfer from the gas into the dust via collisions with the same units as heating and cooling, $\mathrm{erg\,s^{-1}\,(gas\ particle)^{-1}}$. The ratio thus indicates the timescale per gas particle over which collisions between gas and dust will equillibrate the gas and dust temperatures in the absence of any other heating

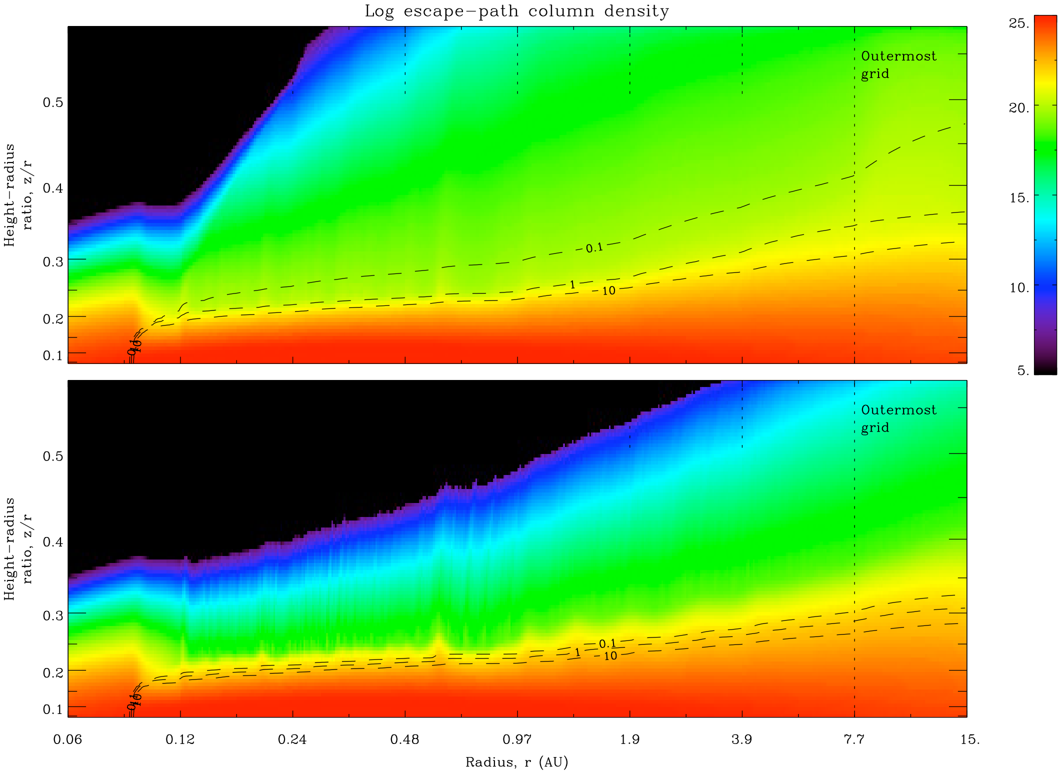

Figure 2.6 The $\log_{10}$ gas particle column density (cm^{-2}) in the direction of smallest optical depth, N_{esc}, for an unsettled disk and a settled disk is plotted as in Figure 2.4.

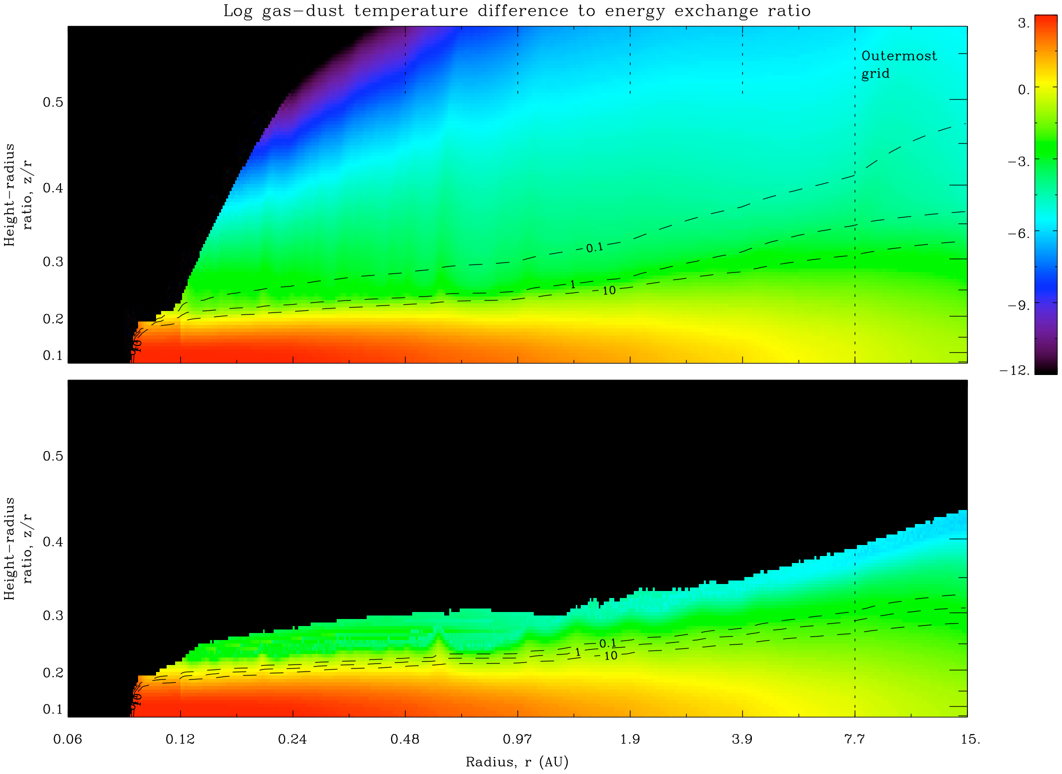

Figure 2.7 The $\log_{10}$ of the collisional energy exchange dust-to-gas / gas-to-dust for all locations within an unsettled and a settled disk is plotted as in Figure 2.4. The gas and dust temperatures are coupled where the gas is densest and where dust exists in abundance.

and cooling mechanisms. The ratio is always positive since $T_{\rm g} > (<) T_{\rm d} \implies \Gamma_{\rm g-d} > (<) 0$.

A ratio of unity indicates that the energy difference between gas and dust in temperature units is comparable to the energy exchange between gas and dust over the duration of 1 second. The coupling between gas and dust in this region of the disk, i.e. near the disk photosphere, can signficantly influence the gas temperature. The gas and dust temperatures are highly coupled (ratio value $\gg 1$) beneath the disk photosphere where the gas is dense and dust exists so that the dust heating and cooling regulates the gas temperature. Where the gas is least dense and/or where dust does not exist, i.e. above the disk photosphere, gas and dust are decoupled (ratio value $\ll 1$) so that gas heating and cooling regulates the gas temperature.

Chapter 3

Radiation field

Pisco calculates the radiation field due to stellar radiation and dust reprocessing at each point within the disk via 3D ray tracing across a span of wavelengths from $\sim$0.1 to just short of 1000 μm. 3D radiative transfer is necessary to account for radiative coupling between areas of an actual protoplanetary disk that are separated in azimuthal distance. The calculations do not include any radiation emitted by gas but only stellar radiation and radiation from warm dust. The calculated mean intensity at 0.1, 10, and 866 μm is plotted in Figs 3.1, 3.2, 3.3.

The radiation field has not diffused through the innermost grid because a higher grid cell resolution is used for the innermost grid compared to rest of the disk, and calculations of the ray tracing at the grid boundaries show inconsistencies in the radiation field at high optical depths for wavelengths $\lesssim 100\,\mu$m. This inconsistency has consequences for the heating (Chapter 5) and cooling (Chapter 6) of the disk

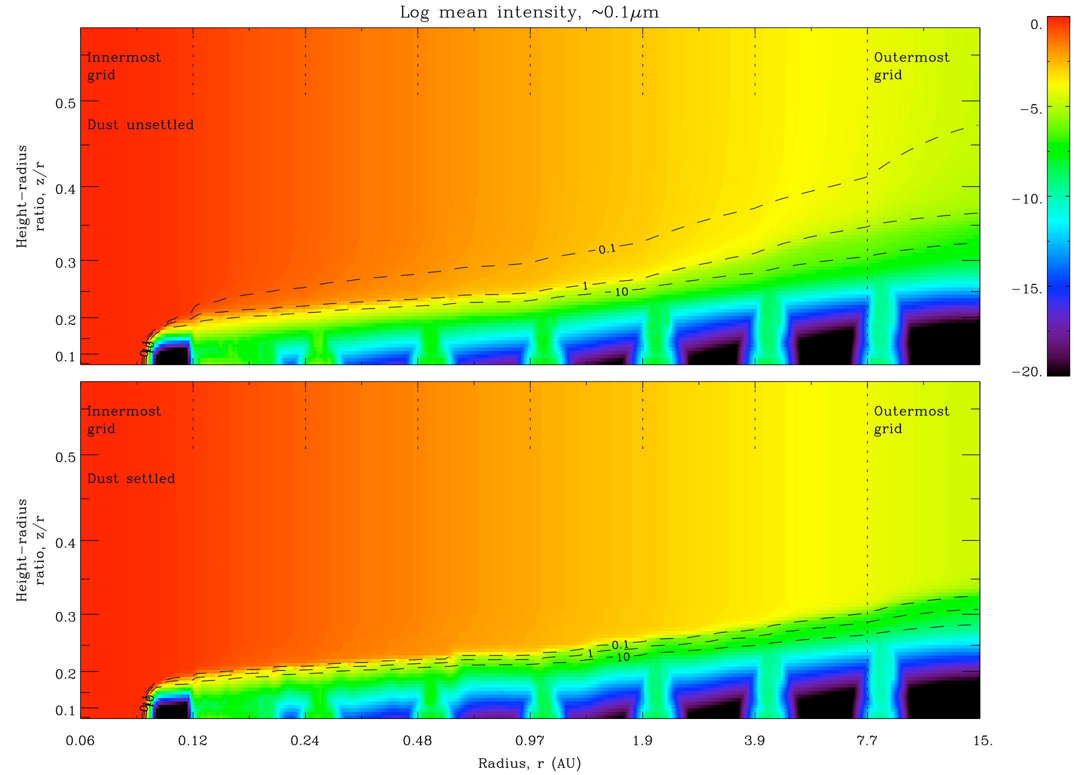

Figure 3.1 The $\log_{10}$ mean intensity of the local radiation field at $\sim 0.1\,\mu\mathrm{m}$ for all locations within an unsettled disk and a settled disk are plotted as in Figure 2.4. Units are with respect to wavenumber, $\mathrm{erg\,s^{-1}\,cm^{-2}\,sr^{-1}\,(cm^{-1})^{-1}}$. Radiative transfer calculations by ray tracing suffer inconsistencies at grid boundaries where optical depth is high. Ultraviolet radiation originates from accretion onto the star and is absorbed at the disk photosphere by dust.

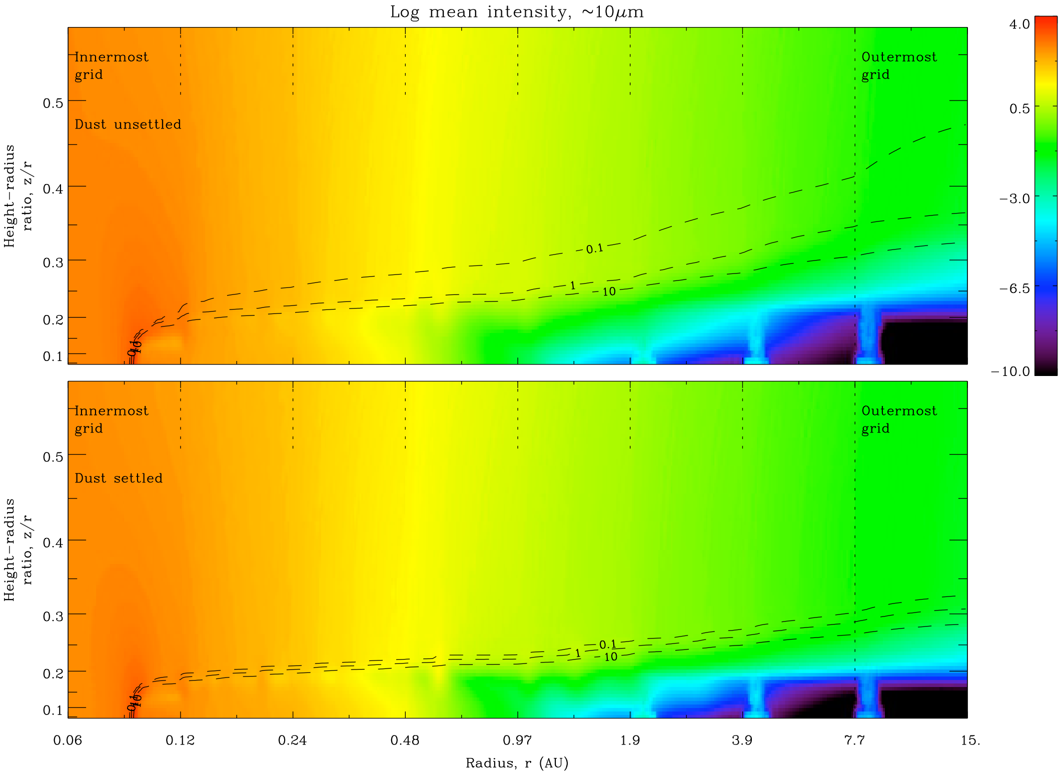

Figure 3.2 The $\log_{10}$ mean intensity of the local radiation field with respect to cm^{-1} at $\sim 10\,\mu\mathrm{m}$ for all locations within an unsettled disk and a settled disk are plotted as in Figure 3.1. Infrared radiation originates from warm dust, and the disk is still optically thick.

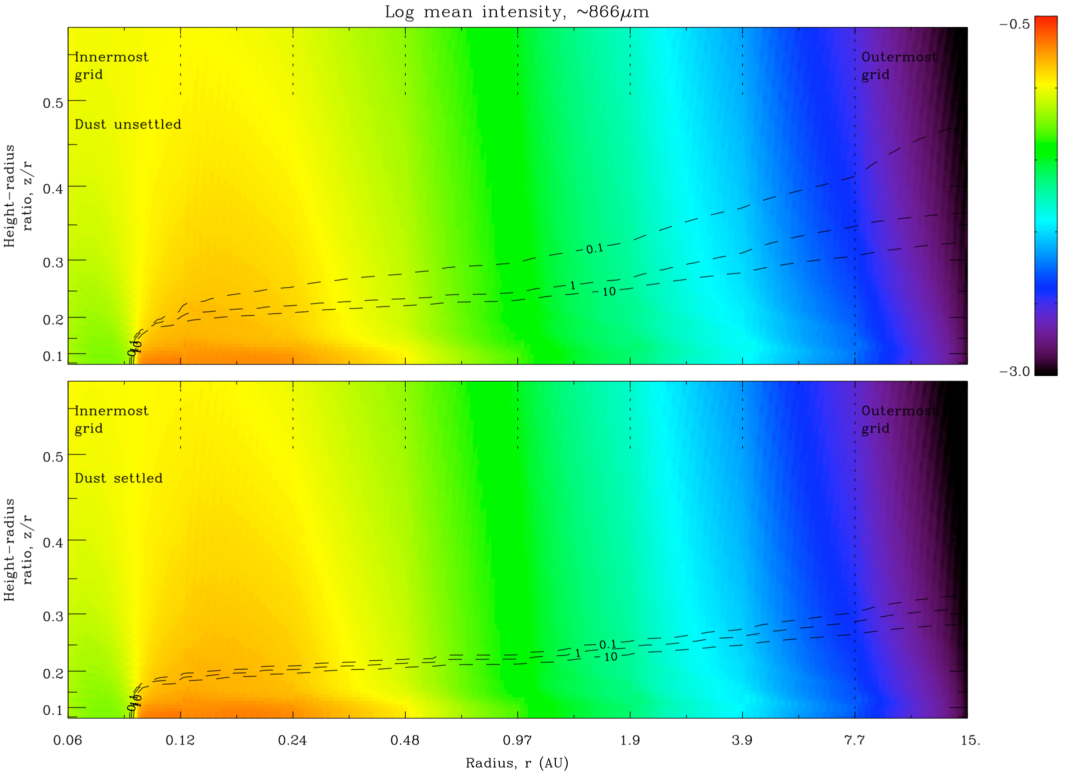

Figure 3.3 The $\log_{10}$ mean intensity of the local radiation field with respect to cm^{-1} at $\sim$866 μm for all locations within an unsettled disk and a settled disk are plotted as in Figure 3.1. Submillimeter radiation originates from dust at the midplane, and the disk is optically thin.

and is partially responsible for the jagged disk structure. But while the radiation field close to the disk midplane is incorrect, the radiation field at and above the disk photosphere shows no inconsistencies across grid boundaries. Pisco is being tested against the benchmarks of Pinte et al. (2009), and Pisco is relevant to the disk photosphere and where radiative effects are significant to the physical conditions.

The ultraviolet radiation (Figure 3.1) originates from accretion onto the star and is absorbed at the disk photosphere by dust. In the infrared (Figure 3.2), the strongest source of radiation is the warm dust of the disk, and the disk is still optically thick. In the submillimeter (Figure 3.3), the dust closest to the midplane is the strongest source of radiation and the disk is optically thin. The local radiation field for both the unsettled and settled cases of the disk shows little difference at all wavelengths.

Chapter 4

Abundances

Abundances of ionized, atomic, and molecular species within the disk control the heating and cooling due to those species. Abundance values in this thesis are relative to the total number of hydrogen gas atoms in both atomic and molecular forms. For the calculation of cooling via emission by molecules, the abundances assumed within Pisco are constant wherever the gas temperature is greater than the freeze-out temperature, Table 4.1. The cooling due to molecular emission above the disk photosphere is overestimated as a result (Chapter 6). In contrast, abundances necessary for the calculation of cooling via emission from forbidden transitions of singly ionized carbon, [CII], and neutral oxygen, [OI], are adapted from Glassgold et al. (2004, Figs 4, 5). Because of the inconsistency in abundance assumptions between molecular and atomic/ionized cooling processes, the plots of gas cooling show abrupt boundaries where cooling processes are calculated to be more or less

Table 4.1. Assumed molecular abundances for emission from molecules

Species	Abundance [a]	$T_{\text{freeze-out}}$ (K) [b]
H_2	0.5	N/A [c]
CO	10^{-4}	30
H_2O	10^{-4}	150

[a] relative to the total number of hydrogen gas atoms in both atomic and molecular form

[b] abundance assumed 0 for $T_{\text{gas}} \leq T_{\text{freeze-out}}$

[c] $T_{\text{gas}} > T_{\text{freeze-out}}$ for H_2 throughout the disk model

dominant.

For a given abundance, the vertical column density at which that abundance is calculated to occur from Glassgold et al. (2004) is assumed to be 10 times less than the escape-path column density, N_{esc} (Figure 2.6), at which that abundance occurs within Pisco's disk model. This approximation is inaccurate in that the vertical column density from Glassgold, Najita, & Igea, which is for a fixed radius from the central star at 1 AU, is more accurately adapted to Pisco's model by using N_ρ in place of N_{esc}. From Chapter 2, $N_{\text{esc}} \lesssim N_z$, and consequently abundances are overestimated radially and underestimated vertically. Nevertheless, the dominance of abundnaces with respect to general locations below, at, and above the disk photosphere as discussed in this thesis is relevant.

From Figs 4.1 and 4.2, atomic hydrogen dominates the gas abundance above the disk photosphere. Below the disk photosphere, H_2 dominates the gas abundance

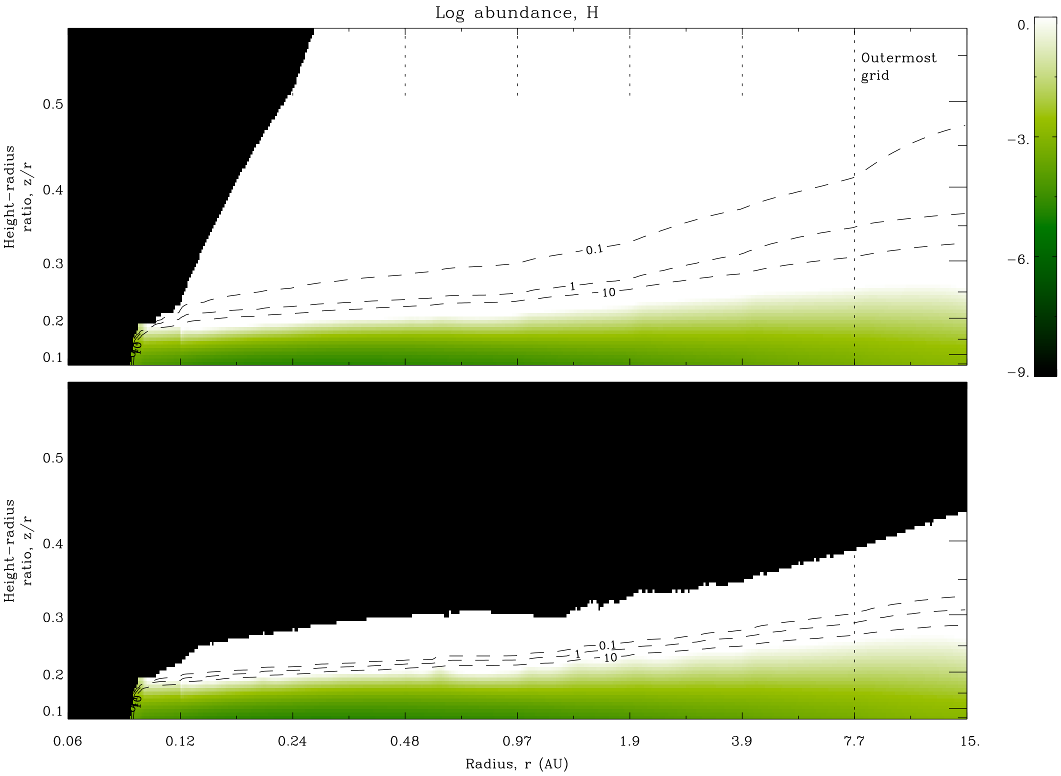

Figure 4.1 The local $\log_{10}$ abundance of atomic hydrogen gas, H, is plotted relative to the total number of hydrogen gas atoms in both atomic and molecular forms for an unsettled disk and a settled disk as in Figure 2.6. H dominates the gas abundance above the disk photosphere.

as H has combined to form H_2. The H_2 abundance is not monotonic with decreasing z/r but drops by an order of magnitude near the disk photosphere before rising to unity.

Electron-CII collisions dominate the collisional excitations leading to [CII] emission, and similarly proton-OI collisions dominate those for [OI]. Assuming an efficient charge transfer between atomic H and positively ionized particles, the free electron abundance is assumed to be equal to the free proton abundance for Pisco's

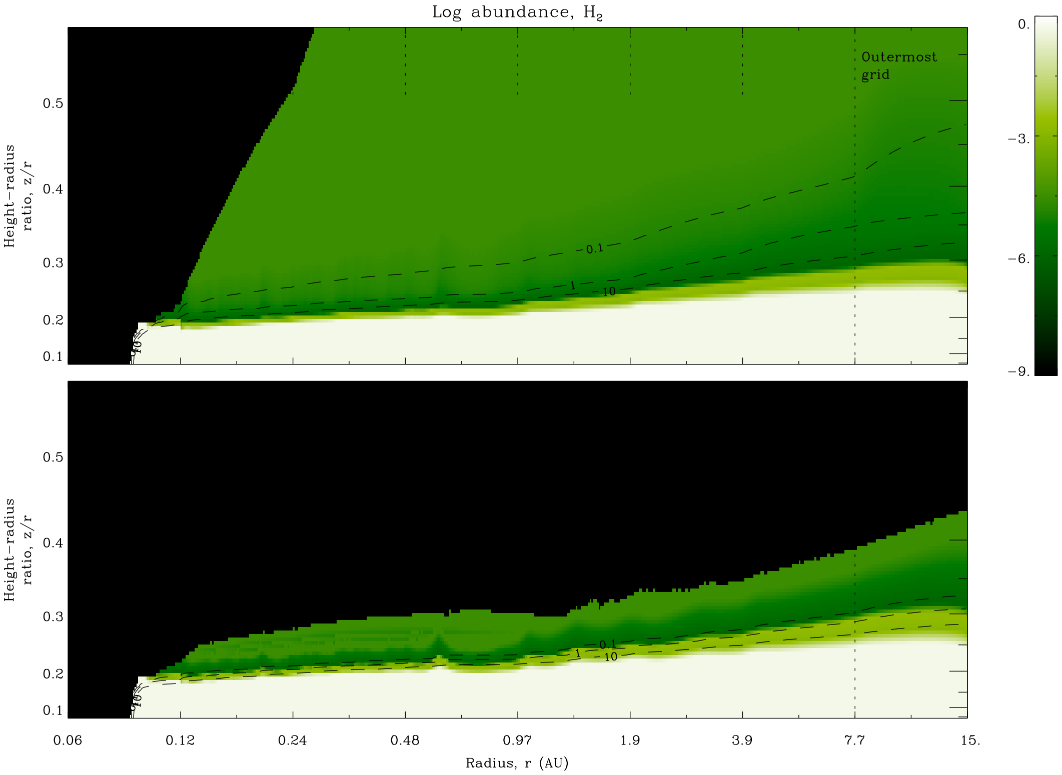

Figure 4.2 The local $\log_{10}$ abundance of molecular hydrogen gas, H_2 is plotted relative to the total number of hydrogen gas atoms in both atomic and molecular forms for an unsettled disk and a settled disk as in Figure 4.1. H_2 dominates the gas abundance below the disk photosphere.

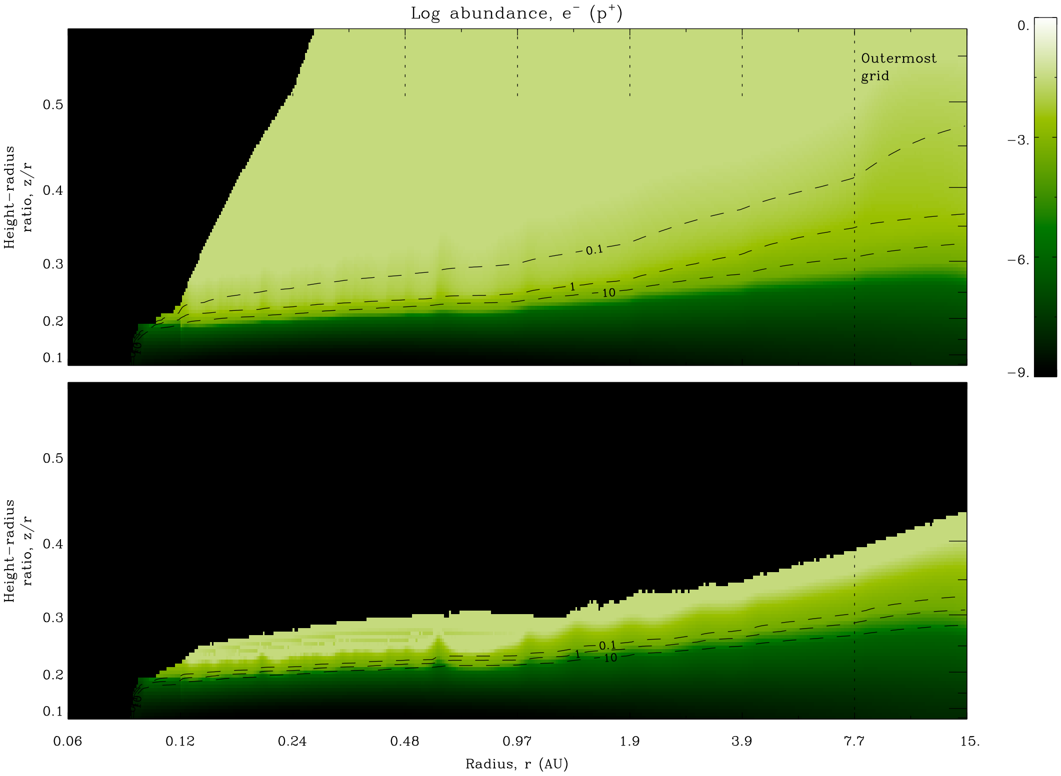

Figure 4.3 The local $\log_{10}$ abundance of free electrons e^- (protons p^+) is plotted relative to the total number of hydrogen gas atoms in both atomic and molecular forms for an unsettled disk and a settled disk as in Figure 4.1. Free electrons and protons are abundant above the disk photosphere.

calculations of the [CII] and [OI] emission. From Figure 4.3, the electron (proton) abundance drops sharply to 10^{-6} below the disk photosphere, which is where H forms H_2.

For calculating cooling by [CII] emission, the CII abundance drops to 10^{-6} just below the disk photosphere. For calculating the cooling by [OI] emission, the OI abundance drops to 10^{-6} deeper within the disk compared to CII. As with CII, OI is also most abundant above the disk photosphere, but beneath the disk photosphere

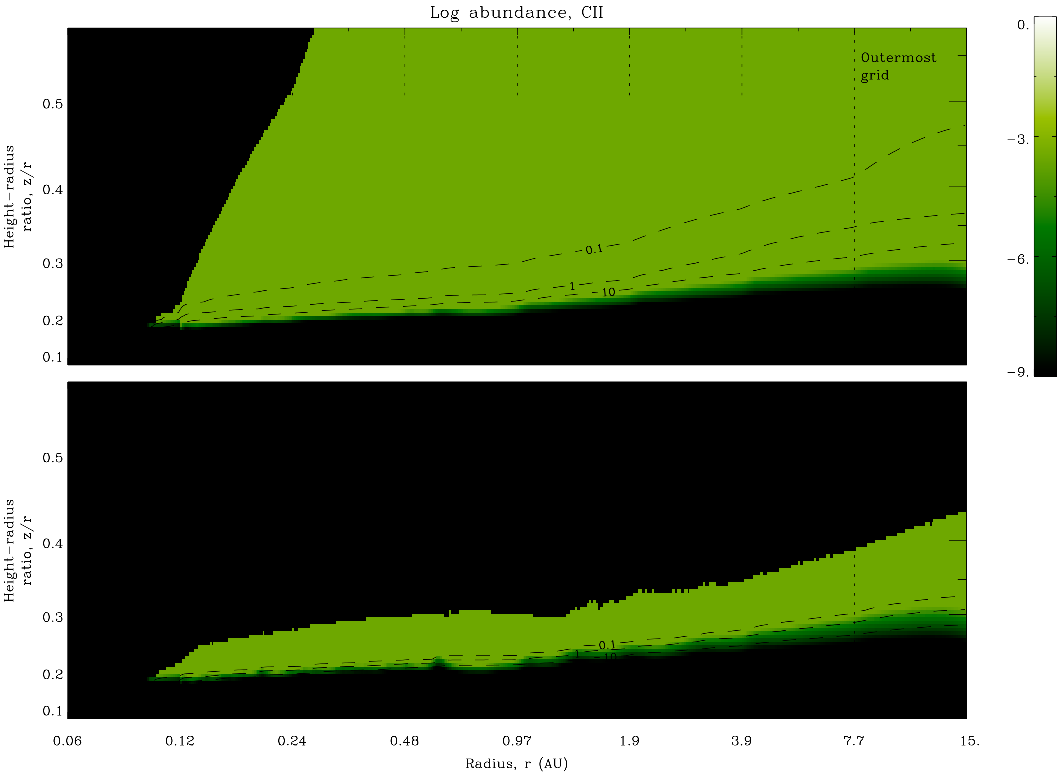

Figure 4.4 The local $\log_{10}$ abundance of singly ionized carbon gas, CII, is plotted relative to the total number of hydrogen gas atoms in both atomic and molecular forms for an unsettled disk and a settled disk as in Figure 4.1. CII is abundant above the disk photosphere.

the abundance of OI does not fall as quickly as that of CII.

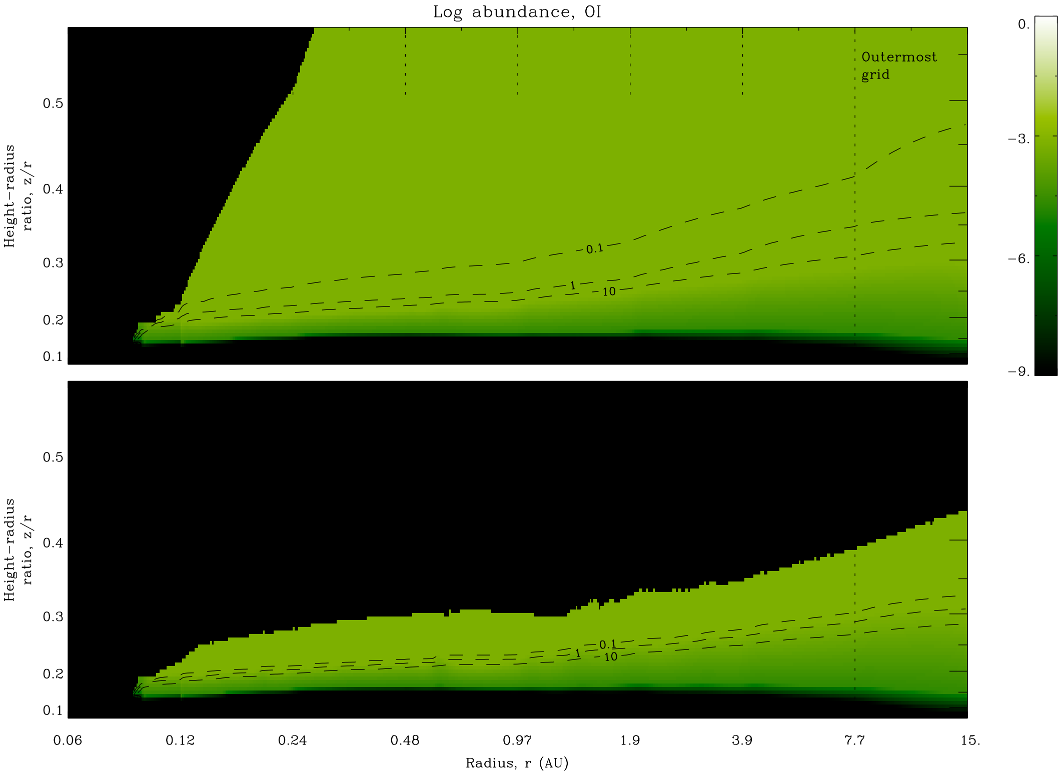

Figure 4.5 The local $\log_{10}$ abundance of neutral atomic oxygen gas, OI, is plotted relative to the total number of hydrogen gas atoms in both atomic and molecular forms for an unsettled disk and a settled disk as in Figure 4.1. OI is abundant above the disk photosphere, but more abundant than CII below the disk photosphere.

Chapter 5

Heating

Temperature is determined via the balance of energy gain (heating) and energy loss (cooling). Because gas comprises over 99% of the disk mass, the gas temperature characterizes the disk temperature. The gas and dust temperatures are coupled at and below the disk photosphere where the gas density is high and dust exists (Chapter 2). In these regions, direct dust heating is mostly responsible for energy flow into the gas and increasing the gas temperature. Conversely, direct gas heating is mostly responsible for increasing the gas temperature where gas and dust are decoupled. All disk heating calculations are in units of $\mathrm{erg\,s^{-1}\,(gas\ particle)^{-1}}$. The total heating, Figure 5.1, is calculated as the sum of direct dust heating and direct gas heating regardless of the potentially coupled or decoupled nature of the gas and dust.

The only direct dust heating mechanism is heating by radiative absorption.

Direct gas heating mechanisms are heating by viscosity, the photoelectric effect, and X-ray absorption. Energy transfer between gas and dust via collisions (an indirect heating/cooling process) is not plotted but is included in the calculation of gas temperature by Pisco. Heating and cooling are not calculated where dust has sublimated, but rather the disk temperature in these regions is assumed to be that of a blackbody (Chapter 2). The temperature calculation boundaries and jagged structure of the disk surface are evident as discussed before, and the effect of inconsistencies in calculating the radiation field along grid boundaries is also evident (Chapter 3). The majority of the heating of the disk is at the inner rim and inside the inner disk within 1 AU, where the dust is optically thick and the gas is densest.

Absorption of stellar radiation by dust is responsible for over 99% of the total disk heating, Figure 5.2. The contribution of heating by dust to increasing the characteristic disk temperature, which is that of the gas, depends upon the gas-dust coupling, c.f. Figure 2.7. Dust heating is most important for increasing the gas temperature below the disk photosphere, where the gas and dust are well coupled, with less importance at the disk photosphere, where the gas-dust coupling is weak. Above the disk photosphere the gas and dust are decoupled. Dust still remains above the photosphere for a disk with unsettled dust, but the heating of the dust is unimportant to the temperature of the decoupled gas. Very little to no dust remains above the photosphere for a disk with settled dust.

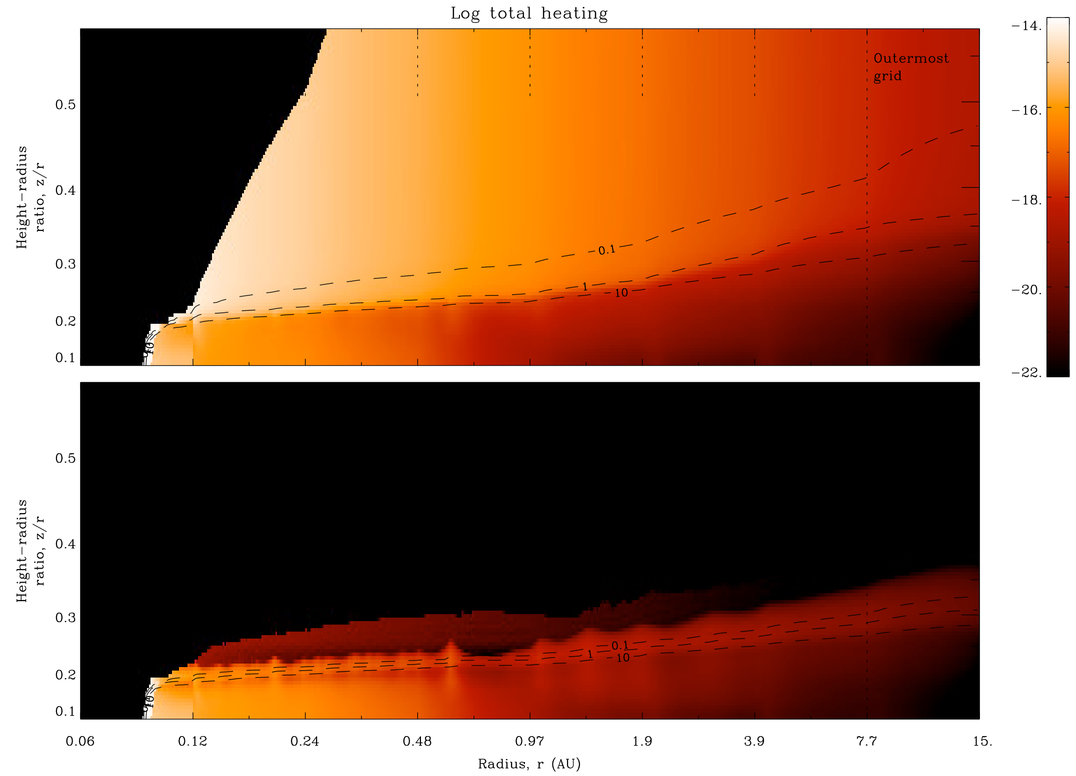

Figure 5.1 The $\log_{10}$ total heating from the disk (erg s^{-1} (gas particle)$^{-1}$) for an unsettled disk and a settled disk is plotted as in Figure 2.4. Most disk heating occurs at the inner rim and within the inner disk.

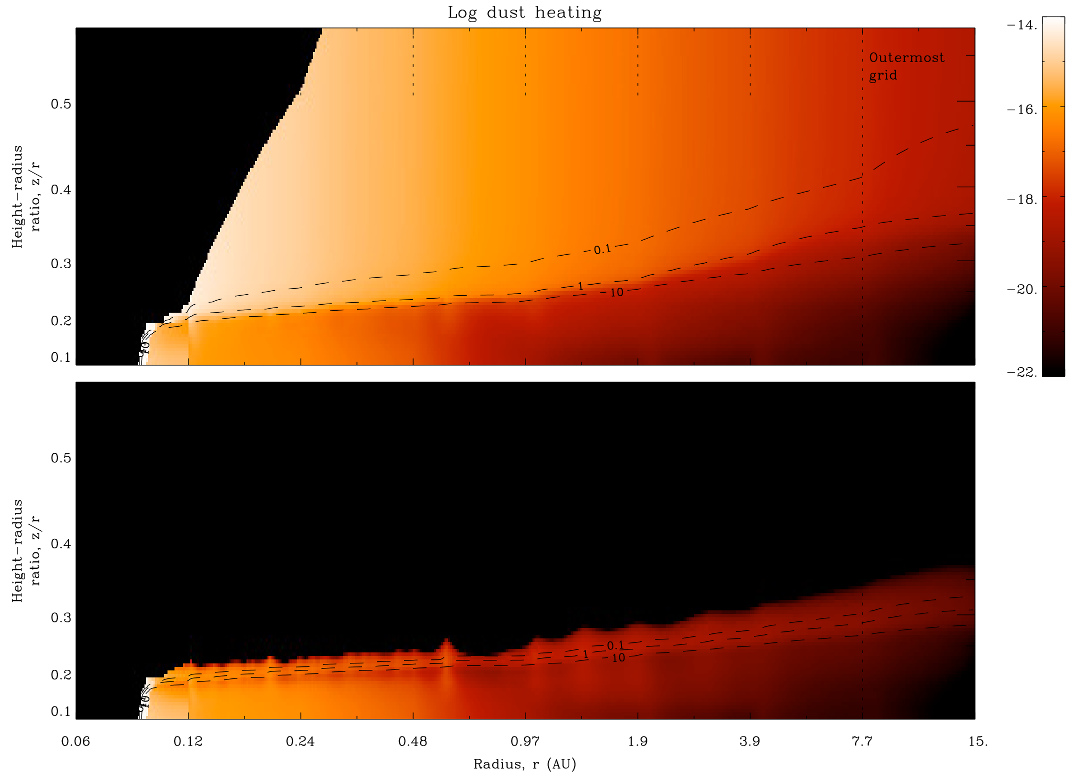

Figure 5.2 The $\log_{10}$ direct dust heating by radiative absorption for an unsettled disk and a settled disk is plotted as in Figure 5.1. Dust heating accounts for over 99% of the total disk heating.

Direct heating of the gas matters most where the gas and dust are weakly coupled or decoupled, i.e. at and above the disk photosphere. The total gas heating is plotted in Figure 5.3 and includes gas heating by viscosity, the photoelectric effect, and X-ray absorption. For the case of a disk with unsettled dust, gas heating is significantly stronger above the disk photosphere than that for a disk with settled dust. The extra gas heating is from the photoelectric effect discussed on page 36. As a result, the gas temperature above the photosphere of the unsettled disk is significantly hotter than that of the settled disk, c.f. Figure 2.4.

The fractional gas heating by a particular process is calculated as the ratio of the heating process to total gas heating. For all plots of fractional gas heating, gas heating processes have not been calculated for the contiguous white area at the top and left of the plot, which is where dust has sublimated and the disk temperature is assumed to be like a blackbody.

Viscous heating, Figure 5.4, is calculated as

$$\frac{\Gamma_{\text{visc}}}{n_{gas}} = \frac{1}{2}\frac{GM_\star \dot{M}}{2\pi\Sigma(r)r^3},$$

where $\Sigma(r)$ is the gas surface density at cylindrical radius r, $\dot{M}$ is the radial mass flux of gas toward the central star, and the factor of 1/2 is from approximating that half of the power goes into heating the gas with the other half assumed to increase the orbital speed of the gas by the virial theorem. Viscous heating is assumed to

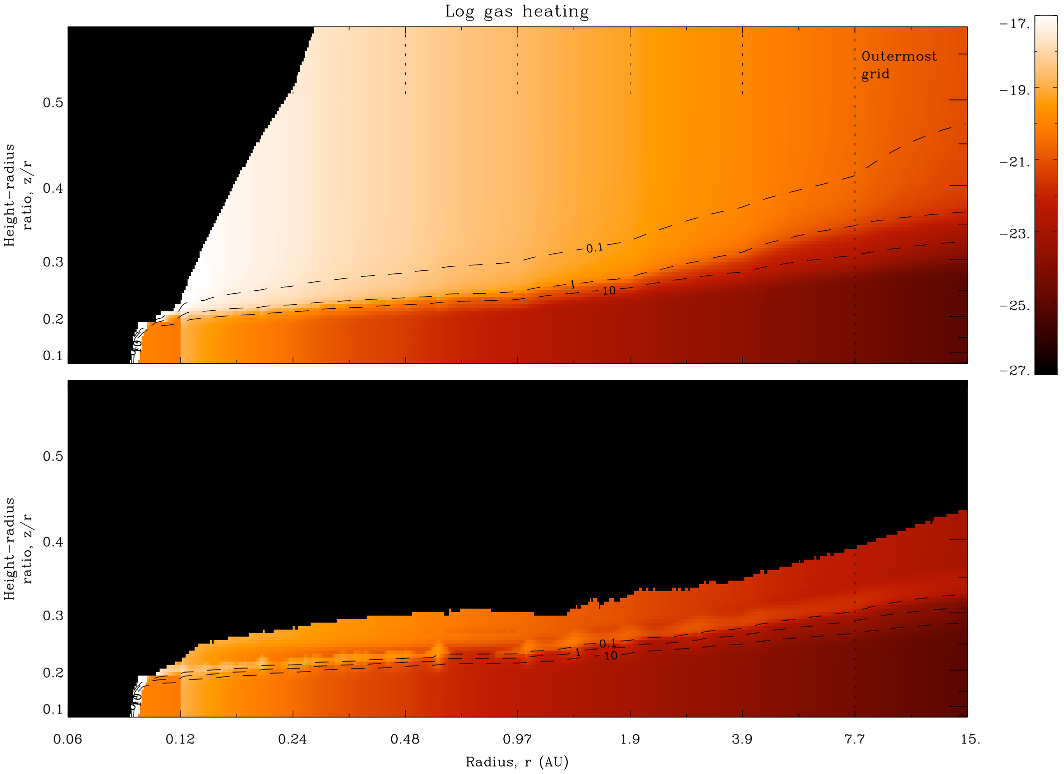

Figure 5.3 The $\log_{10}$ direct gas heating for an unsettled disk and a settled disk is plotted as in Figure 5.1. Gas heating is stronger above the disk photosphere when dust is unsettled.

be constant at all heights above the midplane due to the assumed dependence on the gas surface density rather than the local gas particle density. Because the other calculated direct gas heating mechanisms, the photoelectric effect and X-ray absorption, are both dependent on optical depth effects, and because the gas temperature is assumed to be $\propto r^{-1/2}$ (r as spherical radius) where dust has sublimated, viscous heating dominates direct gas heating only at high optical depths below the disk photosphere. However, energy flow into the gas is dominated by dust heating in these areas of the disk. No calculation of viscous heating has been performed for radii within the disk's inner rim, which is where viscous heating would dominate contributions to the gas temperature, Dullemond et al. (2007).

Photoelectric heating of the gas is calculated as 5% of the dust heating due to ultraviolet absorption per Tielens (2005, pg. 70). The photoelectric effect dominates the heating of the gas at and above the disk photosphere where the ultraviolet radiation has not been attenuated, Figure 5.5. At high optical depths, Pisco's ray tracing calculation of radiative transfer does not accurately calculate the radiation field at grid boundaries and permits scattering down to the midplane. The enhanced penetration of ultraviolet into the disk enhances the photoelectric heating in error. While the gas and dust temperatures are coupled deep within the disk, this extra albeit small amount of gas heating contributes to the instabilities in the disk structure: instabilities that ultimately result in the jagged disk structure (Chapter 2).

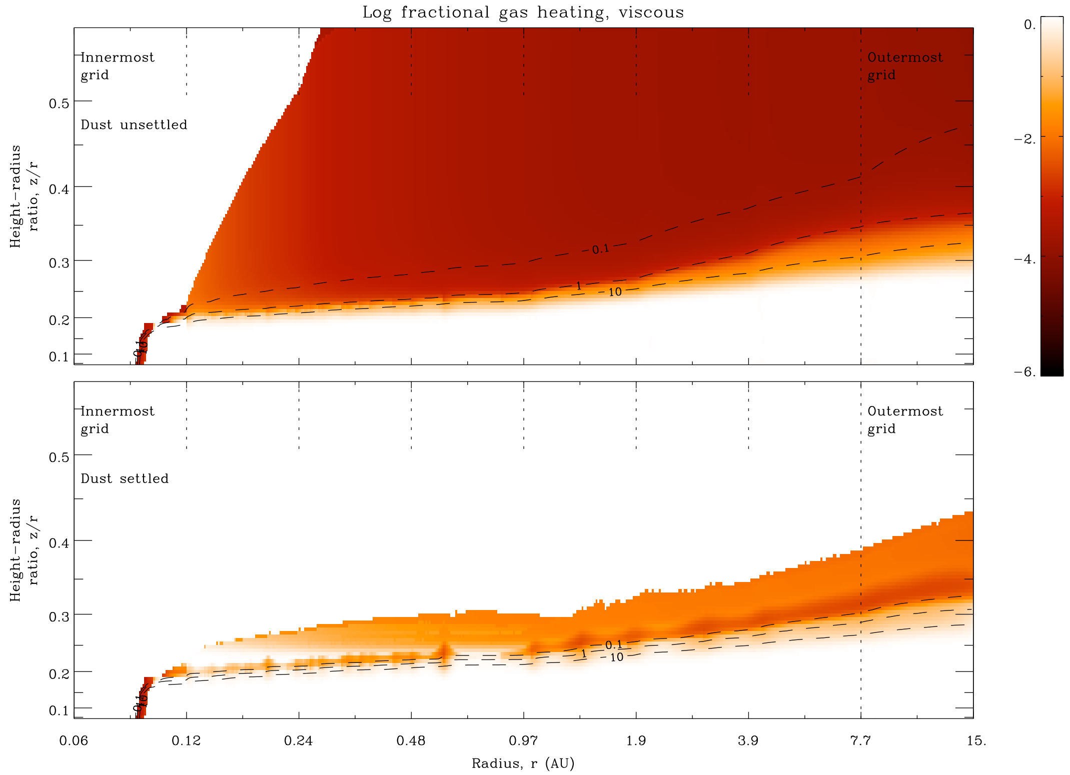

Figure 5.4 The $\log_{10}$ fractional gas heating due to viscosity for an unsettled disk and a settled disk is plotted as in Figure 5.1. The contiguous white area at the top and left of the plot is above the calculated gas temperature boundaries and does not have values for gas heating. Viscous gas heating dominates among direct gas heating mechanisms at high optical depths but contributes little to the gas temperature. Viscous heating is not calculated interior to the disk inner rim.

Because the photoelectric effect is dependent on the presence of dust and ultraviolet radiation, photoelectric gas heating is confined to where dust exists and the stellar line-of-sight optical depth into the disk in ultraviolet is small. The resultant profile for photoelectric heating of the gas resembles the profile for dust heating near the disk photosphere. Settling the dust reduces the presence of dust above the disk photosphere and thus confines photoelectric heating of the gas to the disk photosphere. With the gas and dust decoupled only above the disk photosphere, the photoelectric heating of the gas is primarily responsible for contributions to the temperature only in the case of a disk with unsettled dust. The photoelectric gas heating as a result of unsettled dust leads to a high gas temperature above the disk photosphere.

X-ray heating of the gas is calculated as

$$\frac{\Gamma_{\mathrm{Xr}}}{n_{\mathrm{gas}}} = \frac{L_{\star,\mathrm{Xr}}}{4\pi r^2} \frac{\frac{\sigma_{\mathrm{H,Xr}}}{2}}{(\frac{\sigma_{\mathrm{H,Xr}} N_\rho}{2} + 1)^2},$$

where $L_{\star,\mathrm{Xr}} \approx 10^{-4} L_\star$ is the X-ray luminosity of the star, N_ρ is the radial gas column density in spherical coordinates, and $\sigma_{\mathrm{H,Xr}}$ is the X-ray absorption cross-section in $\mathrm{cm}^{-2}\,\mathrm{H}^{-1}$. The X-ray spectrum is adapted from Gorti & Hollenbach (2008) as a power law with a single absorption cross-section $\sigma_{\mathrm{H,Xr}} \approx 10^{-22}$. In contrast to photoelectric gas heating, X-ray absorption dominates the gas heating above the disk photosphere where dust does not exist, Figure 5.6. Where the gas and dust are

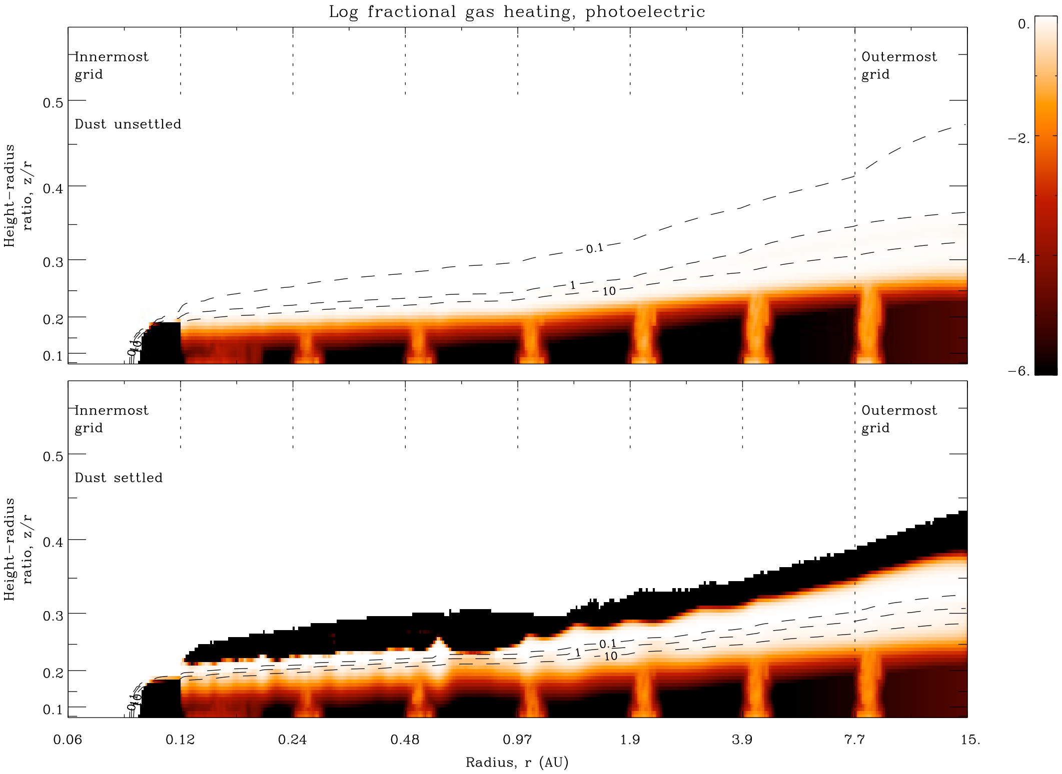

Figure 5.5 The $\log_{10}$ fractional gas heating due to the photoelectric effect for an unsettled disk and a settled disk is plotted as in Figure 5.4. Photoelectric gas heating significantly increases the gas temperature above the disk photosphere when dust is unsettled.

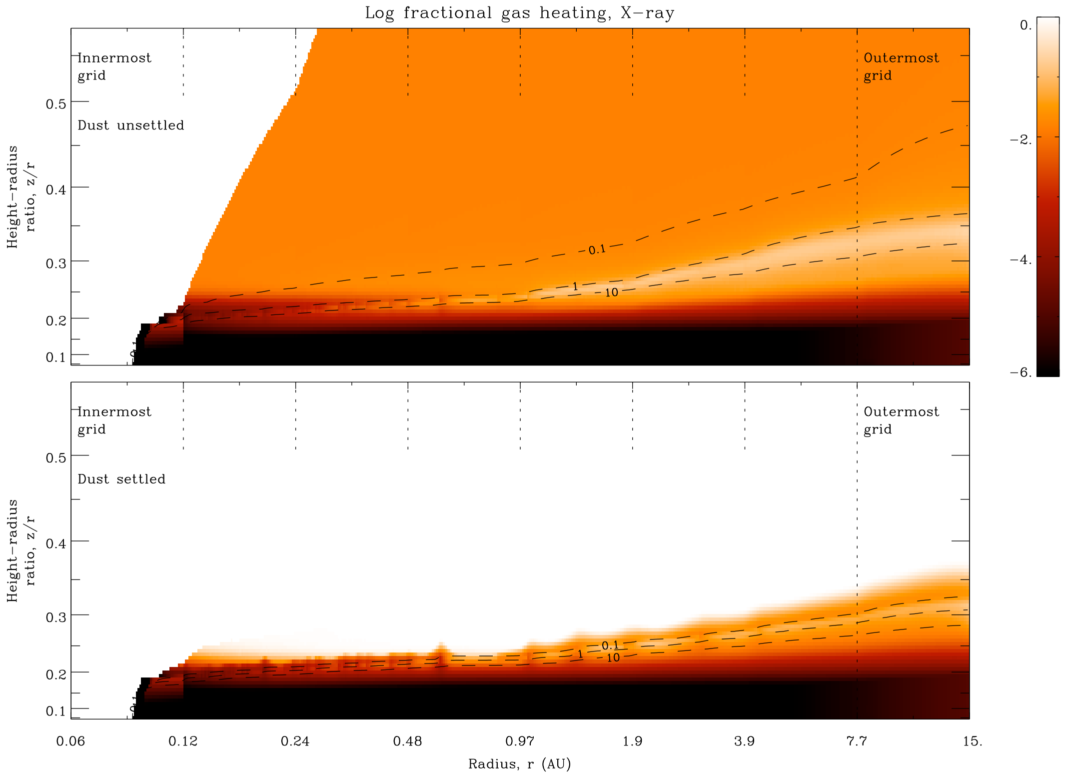

Figure 5.6 The $\log_{10}$ fractional gas heating due to X-ray absorption of the gas for an unsettled disk and a settled disk is plotted as in Figure 5.4. X-ray absorption is the dominant gas heating mechanism above the disk photosphere when dust is settled.

decoupled above the disk photosphere, photoelectric gas heating dominates contributions to the gas temperature in the case of a disk with unsettled dust, whereas gas heating by X-ray absorption dominates contributions to the gas temperature in the case of a disk with settled dust.

Chapter 6

Cooling

Energy loss from the disk (cooling) reduces the disk temperature. The gas temperature is the characteristic temperature of the disk, and as discussed for heating, the gas temperature is influenced by both direct gas cooling and direct dust cooling by virtue of gas-dust coupling. Disk cooling is in the same units as disk heating, $\mathrm{erg\,s^{-1}\,(gas\ particle)^{-1}}$. The total cooling, Figure 6.1, is again calculated as the sum of direct gas and dust cooling in spite of potential gas-dust coupling.

The only direct dust cooling mechanism is cooling by radiative emission from the dust. Direct gas cooling mechanisms are cooling by emission from the collisionally excited rotational and vibrational transitions of CO, H_2O, and H_2; and by emission from singly ionized carbon (CII) and atomic oxygen (OI). Energy transfer between gas and dust is included within Pisco's calculation of the disk temperature but is not plotted. Disk cooling is not calculated where dust has sublimated, but

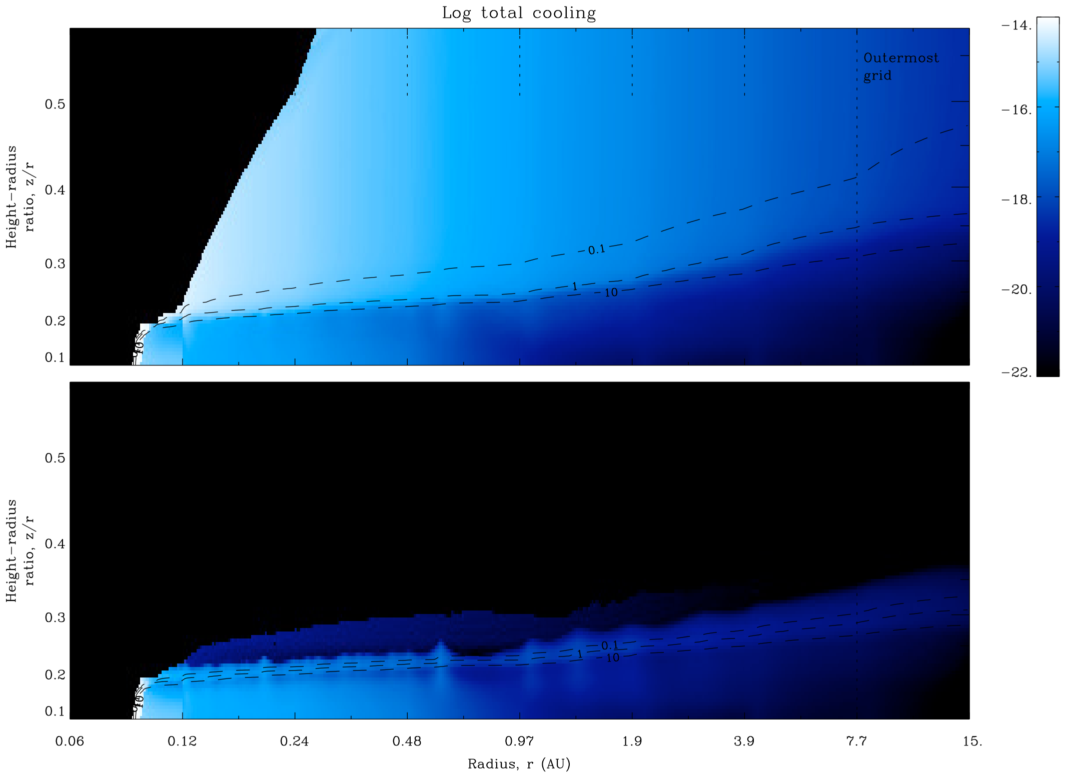

Figure 6.1 The $\log_{10}$ total cooling from the disk (erg s^{-1} (gas particle)$^{-1}$) for an unsettled disk and a settled disk is plotted as in Figure 5.1. Most disk cooling occurs at the inner rim and within the inner disk.

rather the disk temperature is assumed to be that of a blackbody. Boundaries from the temperature calculation, jagged disk structure (Chapter 2), and grid boundaries from radiative transfer (Chapter 3) are again evident. As with the total disk heating, the majority of the disk cooling at the inner rim and inside the inner disk within 1 AU, where the dust is optically thick and the gas is densest.

In mirror of dust heating, emission of radiation by warm dust constitutes over 99% of the total disk cooling, Figure 6.2. Because the contribution of cooling by

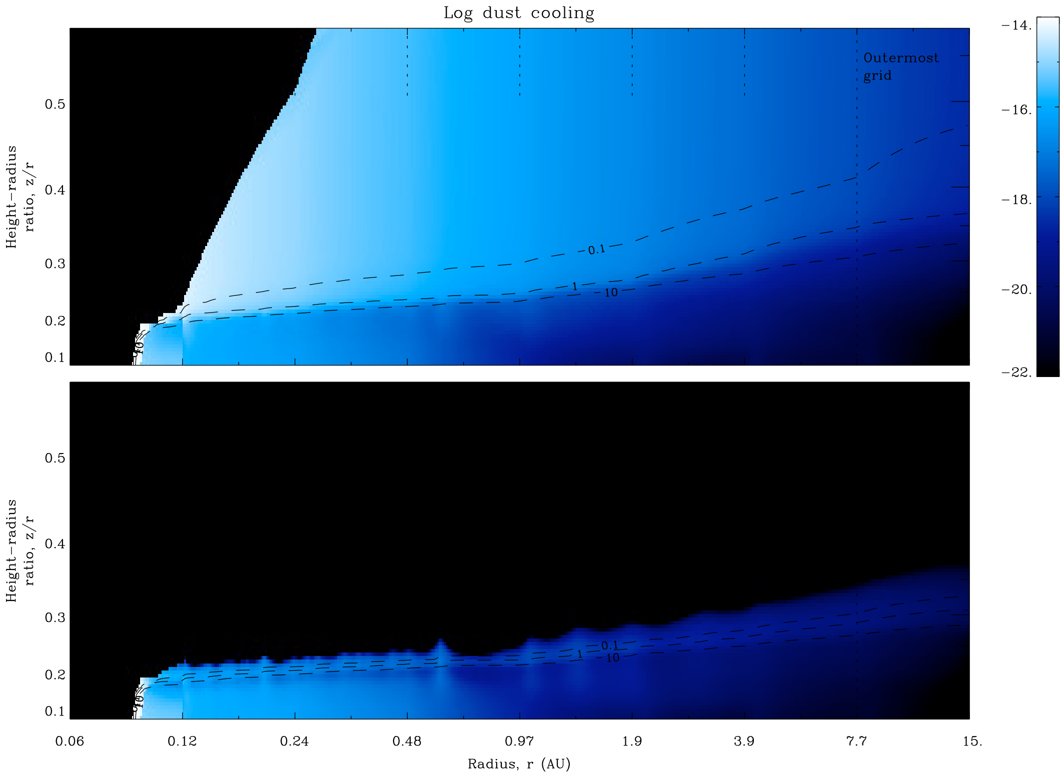

Figure 6.2 The $\log_{10}$ direct dust cooling by emission for an unsettled disk and a settled disk is plotted as in Figure 6.1. Dust cooling accounts for over 99% of the total disk cooling.

dust to decreasing the characteristic disk temperature, i.e. that of the gas, depends on the gas-dust coupling, c.f. Figure 2.7, dust cooling is again most important below the disk photosphere with decreasing importance up to the disk photosphere. Dust cooling is unimportant to the gas temperature above the disk photosphere where the gas and dust are decoupled.

Again, direct cooling of the gas matters most at and above the disk photosphere where gas-dust coupling is weak to none. The total gas cooling is plotted in

Figure 6.3 and includes gas cooling by the rotational and vibrational transitions of CO, H_2O, and H_2; and by emission from CII and OI. Cooling by CO, H_2O, and H_2 has been adapted from (Neufeld & Kaufman, 1993). The molecular transitions are excited by collisions with other gas particles, all assumed to be atomic hydrogen, thereby removing only kinetic energy from the gas. NLTE effects on the cooling by CO, H_2O, and H_2 have been approximated by Neufeld & Kaufman with critical density and escape probability approximations. Pisco does not yet modify the calculated radiation field (Chapter 3) due to NLTE effects by gas coolants, however any changes are expected to be small, c.f. Meijerink et al. (2008). NLTE effects, although found to be insignificant, are also approximated in the calculation of cooling by CII and OI, derived in §§ 6.1-6.3.

Gas cooling will be stronger above the photosphere of a disk with unsettled dust due to increased heating and thus a higher gas temperature (c.f. page 34), but the cooling due to molecular transitions has been overestimated in these calculations by assuming a constant molecular abundance, except where molecules are frozen out of the gas (Chapter 4). From Glassgold et al. (2004, Fig 5), the abundances of CO and H_2O should fall off to 10^{-10} at about the top of the disk photosphere. Above the disk photosphere, the calculated emission of CO and H_2O is overestimated and should be ignored. H_2 abundance should fall off as in Figure 4.2 and should thus be reduced by a significant factor. In addition, because the abundances of CII and OI and the associated collisional species are inconsistent with the constant abundances assumed for the molecular gas cooling processes, there are abrupt boundaries where gas cooling processes jump in dominance by Pisco's calculation.

As with gas heating, the fractional gas cooling by a particular process is calculated as the ratio of the cooling process to total gas cooling. For all plots of fractonal gas cooling, gas cooling processes have not been calculated for the contiguous white area at the top and left of the plot, which is where dust has sublimated and the disk temperature is assumed to be that of a blackbody (c.f. Chapter 2).

Emission from CO rotational transitions is present throughout the disk, Figure 6.4, but the emission dominates other gas cooling mechanisms close to the disk midplane where high column densities reduce the OI abundance and at temperatures sufficiently low to freeze water out of the gas. However, the CO cooling is innately weak due to the cold temperatures. Cooling from dust emission is primarily responsible for reducing the gas temperature at these depths within the disk due to the gas-dust coupling. The strength of CO rotational emission from an unsettled disk is calculated to be similar to that of a settled disk. The rotational CO emission is in the far-infrared to submillimeter and is conspicuous to observations since the disk is optically thin at these wavelengths (e.g. Gorti et al., 2011).

The emission from CO vibrational transitions is most prominent where the

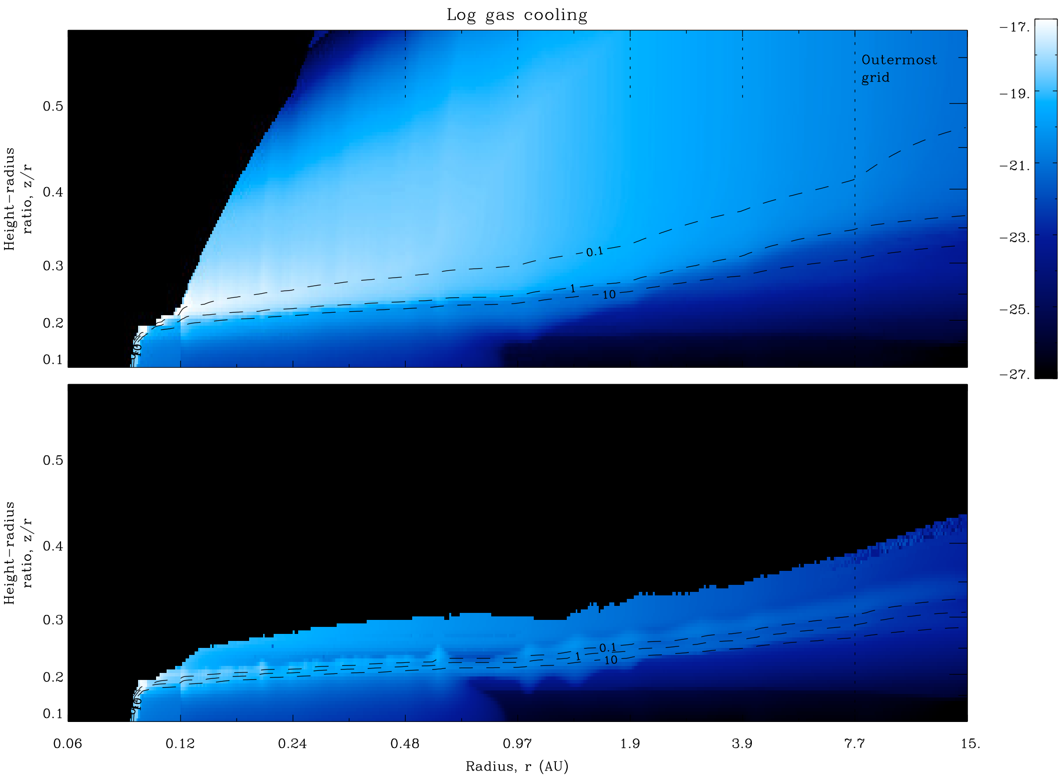

Figure 6.3 The $\log_{10}$ direct gas cooling for an unsettled disk and a settled disk is plotted as in Figure 6.1. Gas cooling is stronger above the disk photosphere when dust is unsettled, but the strength of the cooling and resultant emission calculated here is overestimated.

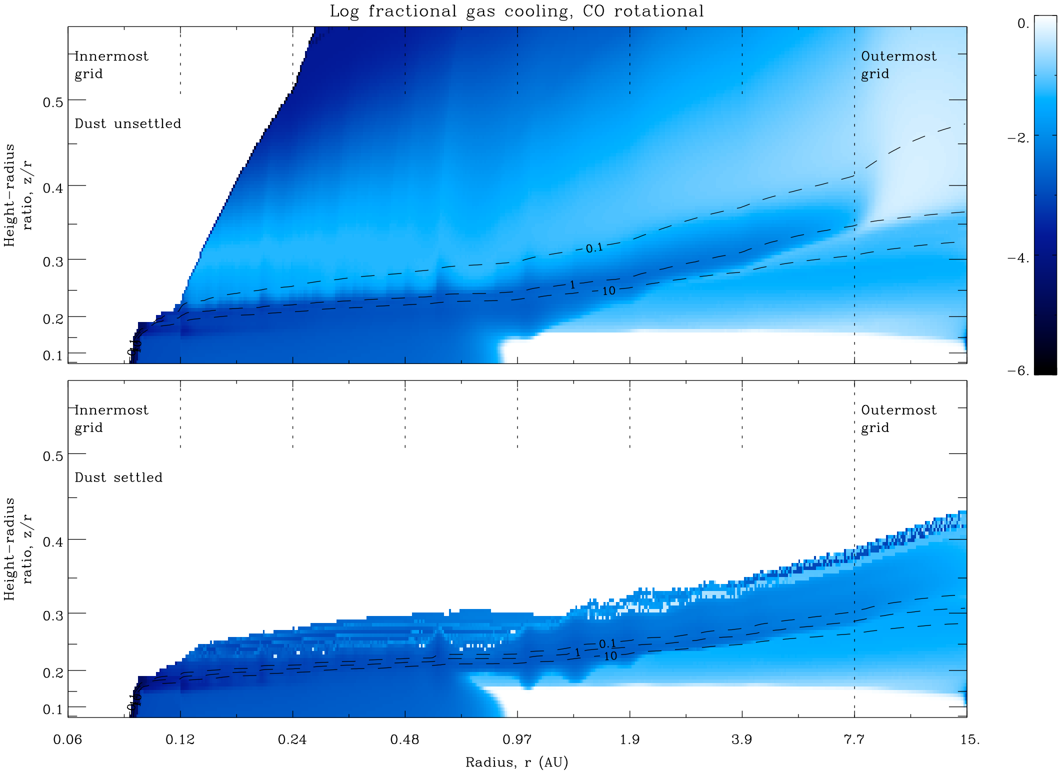

Figure 6.4 The $\log_{10}$ fractional gas cooling due to rotational CO emission in the far-infrared to submillimeter for an unsettled disk and a settled disk is plotted as in Figure 6.3. Emission above the disk photosphere should be ignored. There is little change in the total amount of emission from CO rotational transitions comparing unsettled and settled disks.

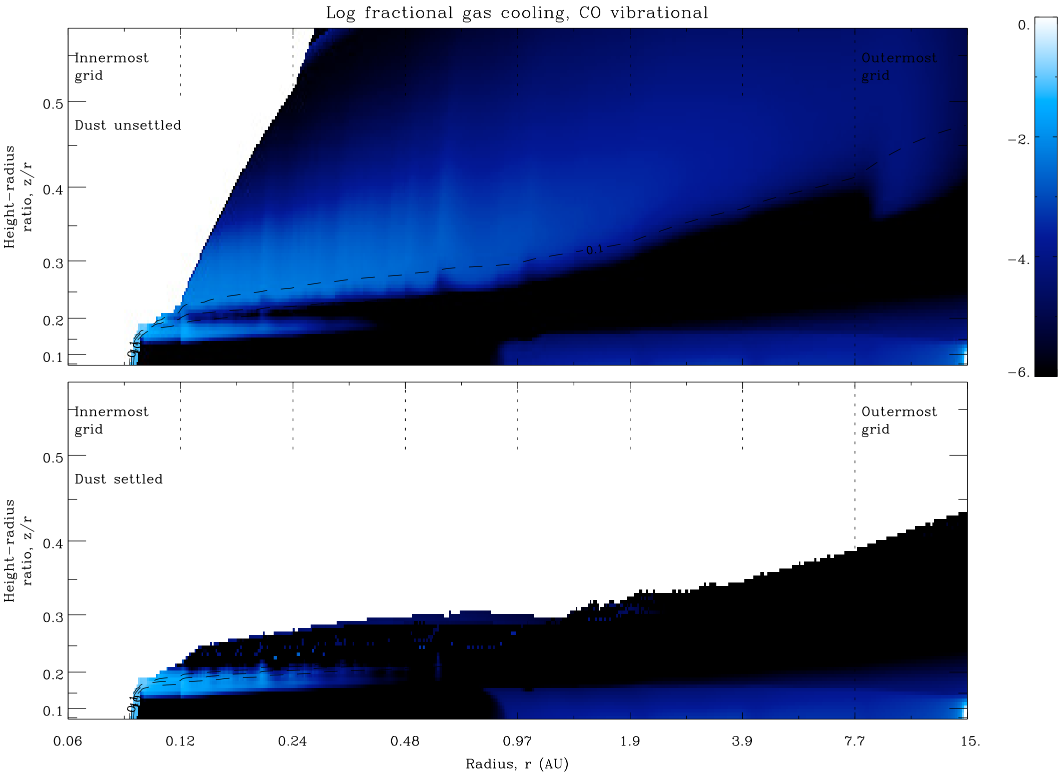

Figure 6.5 The $\log_{10}$ fractional gas cooling due to vibrational CO emission in the near-infrared for an unsettled disk and a settled disk is plotted as in Figure 6.4. Emisson above the disk photosphere should be ignored. There is little change in the total amount of emission from CO vibrational transitions comparing unsettled and settled disks.

gas is hottest ($\gtrsim$ 1000 K), Figure 6.5. For both settled and unsettled disks, the emission is brightest at the inner rim but where gas and dust are coupled. The strength of emission from an unsettled disk is calculated to be similar to that of a settled disk. Being in the near-infrared and from the optically-thin disk surface, emission from the disk is observed (e.g. Pontoppidan et al., 2008).

Rotational water transitions dominate gas cooling wherever water is not

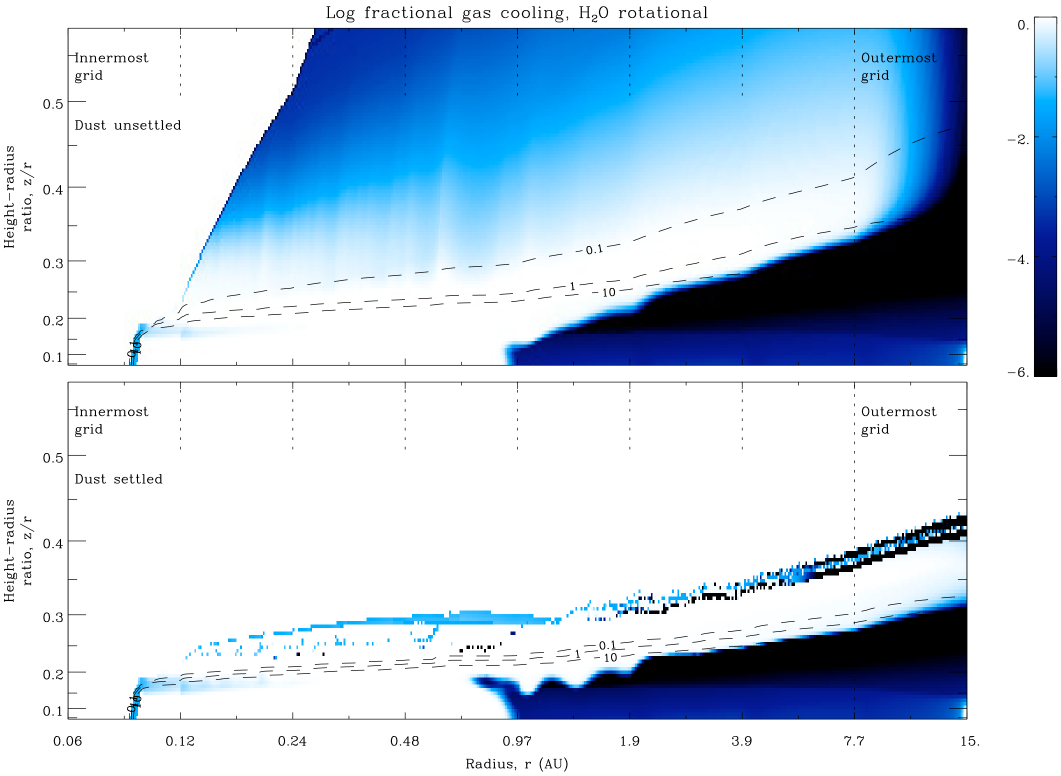

Figure 6.6 The $\log_{10}$ fractional gas cooling due to rotational H_2O emission in the far-infrared for an unsettled disk and a settled disk is plotted as in Figure 6.4. Emission above the disk photosphere should be ignored. As calculated, there is little change in the total amount of emission from water rotational transitions comparing unsettled and settled disks.

frozen out of the gas and except at the inner rim, Figure 6.6. There is little change in the total cooling from rotational water transitions between cases of dust settling. Emission from rotational water transitions in the mid- and far-infrared has been observed (Pontoppidan et al., 2010).

Like emission from CO vibrational transitions, emission from the vibrational transitions of water are also most prominent where the gas is warmest ($\gtrsim 300\,\mathrm{K}$),

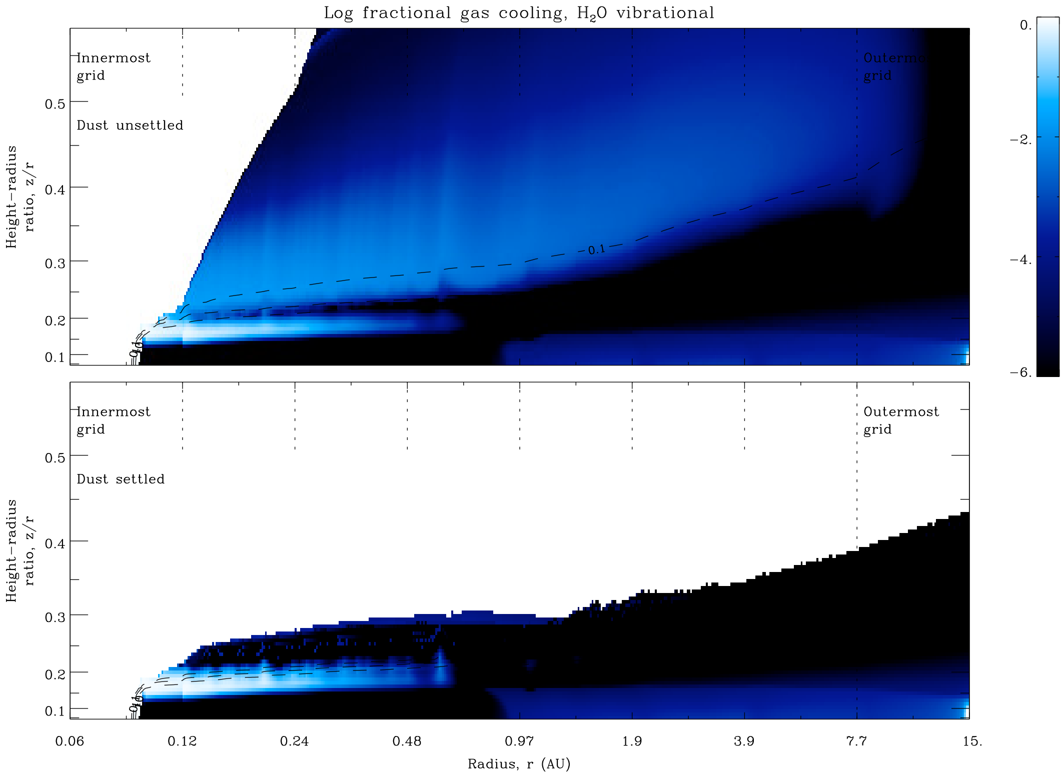

Figure 6.7 The $\log_{10}$ fractional gas cooling due to vibrational H_2O emission in the near-infrared for an unsettled disk and a settled disk is plotted as in Figure 6.4. Emission above the disk photosphere should be ignored. As calculated, there is little change in the total amount of emission from water vibrational transitions comparing unsettled and settled disks.

Figure 6.7. For both settled and unsettled disks, the emission is brightest at the inner rim and just below the disk photosphere but where gas and dust are coupled. The total emission from both types of disks is calculated to be comparable. Being in the near-infrared and from the optically-thin disk surface, emission from the disk is observed (Salyk et al., 2008; Carr & Najita, 2008).

Compared to CO and H_2O, H_2 has a much larger abundance above the disk photosphere. While Pisco's calculation of the gas cooling by molecular emisson has been overestimated because of high abundance assumptions, emission from H_2 will still dominate the gas cooling over that from CO and H_2O. Emission from the rotational transitions of H_2, Figure 6.8, is important to the gas cooling starting at the disk photosphere, where gas and dust are weakly coupled, and becomes more important with increasing height above the disk photosphere. Because the gas above the disk photosphere is hotter in the case of unsettled dust, the total H_2 rotational emission is stronger from an unsettled disk. H_2 rotational emission from some disks in the mid-infrared has been detected (e.g. Bitner et al., 2008).

Emission from H_2 vibrational transitions, Figure 6.9, is important to the gas cooling above the disk photosphere, as with H_2 rotational emission. Likewise, the total H_2 vibrational emission is stronger from an unsettled disk. H_2 vibrational emission from some disks in the near-infrared has been detected (e.g. Carmona et al., 2008).

Emission from radiative de-excitations of CII and OI has been written into Pisco's calculations of gas cooling. The NLTE calculation of CII and OI cooling includes the removal of kinetic energy from the gas of the disk via collisional excitations with other abundant gas species and an approximation for energy removal from the radiation field of the disk via radiative excitations. Incorporating radiative effects into the calculation of CII and OI cooling is inconsequential to the resultant

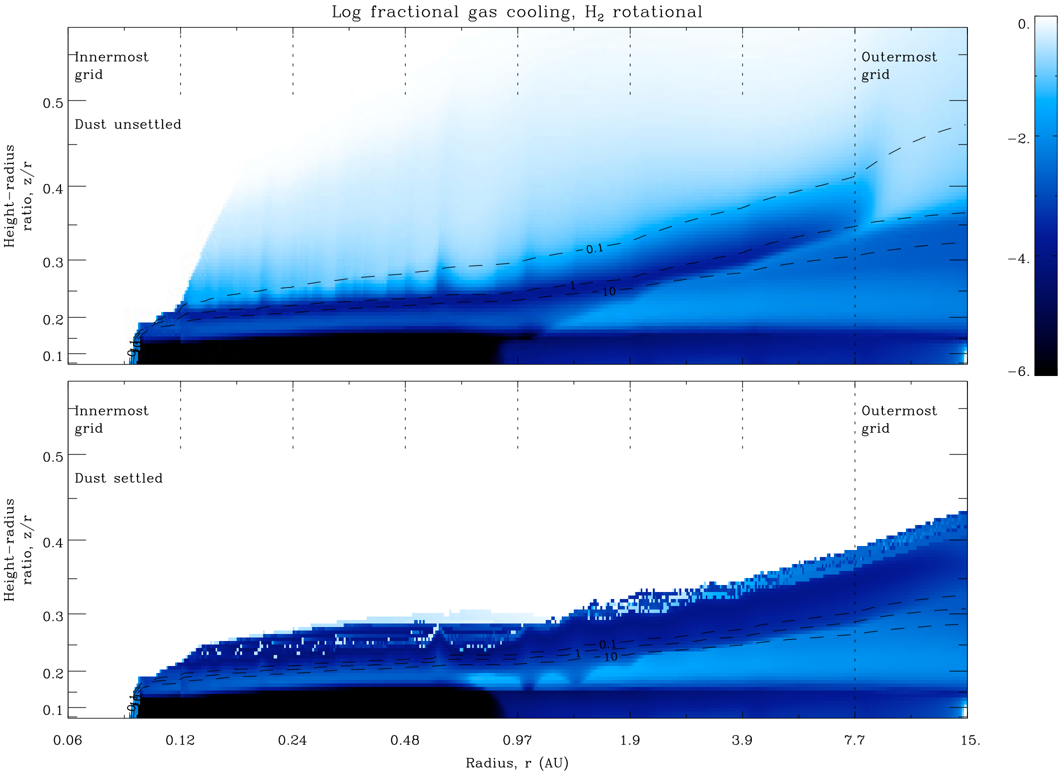

Figure 6.8 The $\log_{10}$ fractional gas cooling due to rotational H_2 emission in the mid-infrared for an unsettled disk and a settled disk is plotted as in Figure 6.4. Emission above the disk photosphere is overestimated, but unsettled disks show stronger H_2 rotational emission compared to settled disks.

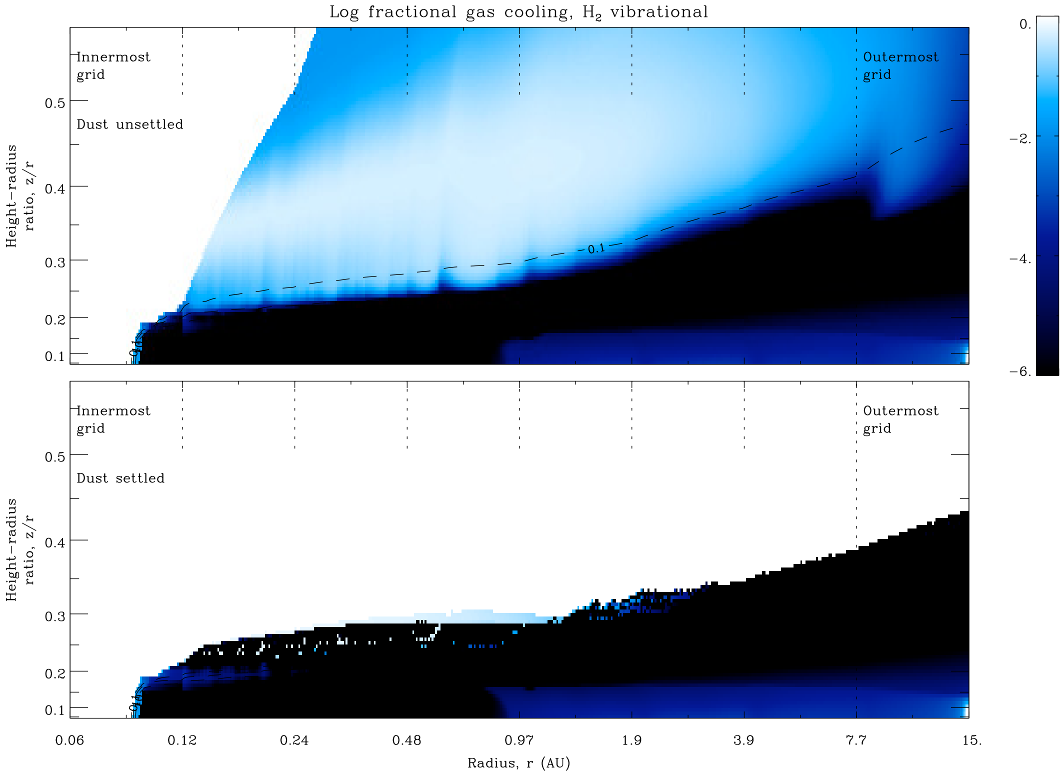

Figure 6.9 The $\log_{10}$ fractional gas cooling due to vibrational H_2 emission in the near-infrared for an unsettled disk and a settled disk is plotted as in Figure 6.4. Emission above the disk photosphere is overestimated, but unsettled disks show stronger H_2 vibrational emission compared to settled disks.

cooling but is included for completeness. The calculation of NLTE radiative cooling from a k-level gas species is described in § 6.1, and the specification to emission from CII and OI is described in §§ 6.2 and 6.3.

6.1 Cooling from a k-level gas species

The steady-state cooling rate due to an energy level transition from a parcel of gas containing a gas species with k internal energy states is described here. Following Tielens (2005, § 2.2), the radiative energy loss from the gas parcel due to a transition of a given gas species from an upper energy state u to a lower energy state l is

$$\Lambda(\nu_{ul}) = n_u A_{ul} h \nu_{ul} \beta(\tau_{ul})(1 - P(\nu_{ul})/S(\nu_{ul}))$$

in units of $\mathrm{erg\,s^{-1}\,cm^{-3}}$. A_{ul} is the Einstein spontaneous emission coefficient, h is Planck's constant, and ν_{ul} is the frequency of the transition in Hz. $\beta(\tau_{ul})$ is the escape probability of the emitted photon from the gas parcel and is dependent on the optical depth of the gas parcel at the frequency of the transition. $P(\nu_{ul})$ is the background radiation field at the frequency of the transition in flux density units of $\mathrm{erg\,s^{-1}\,cm^{-2}\,sr^{-1}\,Hz^{-1}}$, and $S(\nu_{ul})$ is the source function of the gas parcel at the transition frequency in the same flux density units. The source function is

$$S(\nu_{ul}) = \frac{2h\nu_{ul}^3}{c^2}\left(\frac{g_u n_l}{g_l n_u} - 1\right)^{-1}$$

with c as the speed of light and g_u and g_l as the statistical weights of the upper and lower states respectively. The corresponding upper and lower state population densities of the gas species are n_u and n_l.

The energy state population densities are determined from statistical equilibrium and the conservation of particle number. For arbitrary states i and j over all k states, the rate of particles leaving state i per unit volume equals the rate of particles entering state i per unit volume, and the total number of particles per unit volume regardless of state is fixed:

$$n_i \sum_{j \neq i}^{k} R_{ij} = \sum_{j \neq i}^{k} n_j R_{ji}$$
$$n_{\text{tot}} = \sum_{i}^{k} n_i.$$

The transition rate R_{ij} is that of states $i \to j$, and n_{tot} is the total number density of the gas species regardless of state. Again designating the upper and lower states as u and l respectively, the transition rates are the sum of the radiative and collisional transitions from a state:

$$R_{ul} = A_{ul}\beta(\tau_{ul})(1 + Q(\nu_{ul})) + C_{ul}$$
$$R_{lu} = \frac{g_u}{g_l} A_{lu}\beta(\tau_{lu})Q(\nu_{lu}) + C_{lu}.$$

The Einstein coefficient $A_{ul} = A_{lu}$ is the probability per unit time of a spontaneous transition by absorption ($l \rightarrow u$) or emission ($u \rightarrow l$). Because escape probabilities are dependent on the frequency of the photon, $\beta(\tau_{ul}) = \beta(\tau_{lu})$. $Q(\nu_{ul}) = Q(\nu_{lu})$ is the population of a single mode of the background radiation field at the frequency of the transition, i.e. $Q(\nu_{ul}) = P(\nu_{ul})\, c^2/2h\nu_{ul}^3$. The collisional excitation and de-excitation rates are C_{ul} and C_{lu} respectively.

For arbitrary energy states i and j, C_{ij} is the sum of the product of the volume-normalized probability per unit time that a collision resulting in a (de-)excitation will occur, i.e. the collisional (de-)excitation rate coefficient γ_{ij} in $\mathrm{cm}^3\,\mathrm{s}^{-1}$, and the number density n for all species m involved in the (de-)excitation of the emitting gas species:

$$C_{ij} = \sum_{m}^{\substack{\text{all collisional} \\ \text{partner species}}} (\gamma_{ij} n)_m .$$

The collisional de-excitation rate coefficient γ_{ul} is often taken as a constant or as a power law of temperature as an approximation to quantum-mechanically calculated collisions between the transitioning gas species and selected collisional partner species, c.f. § 6.2. Energy state populations determined solely by collisions are in thermodynamic equilibrium, and thus the collisional (de-)excitation rate coefficients are related by the statistical weights of the upper and lower energy states and a Boltzmann factor,

$$\frac{\gamma_{ul}}{\gamma_{lu}} = \frac{g_l}{g_u} \exp\left(\frac{-h\nu_{ul}}{kT_{\text{gas}}}\right).$$

With R_{ij} explicitly defined, the rate equations of statistical equilibrium can be solved for k states following Rosseland (1926, 1936); White (1961). The rate equations form a linear system where all equations are related by the conservation equation. The matrix-vector product between a matrix of transition rates and a column vector of state number densities can be written as

$$\mathsf{R}\boldsymbol{n} = \mathbf{0}, \text{ where for transitions } i, j \in \{1, \cdots, k\},$$

$$\mathsf{R} = \begin{pmatrix} -\sum_{j\neq 1}^{k} R_{1,j} & R_{2,1} & \dots & R_{k,1} \\ R_{1,2} & -\sum_{j\neq 2}^{k} R_{2,j} & & \vdots \\ \vdots & & \ddots & \\ R_{1,k} & \dots & & -\sum_{j\neq k}^{k} R_{k,j} \end{pmatrix} \text{ and } \boldsymbol{n} = \begin{pmatrix} n_1 \\ \vdots \\ n_k \end{pmatrix}.$$

For given state i, the diagonal element R_{ii} is the sum of transition rates out of state i, chosen by convention to be negative. The upper-triangular elements $\mathsf{R}_{i,j>i}$ and lower-triangular elements $\mathsf{R}_{i,j<i}$ are de-excitation and excitation rates into i, respectively.

Rosseland (1926, 1936) found the general solution for the species number density in energy state i to be

$$n_i = \lambda_j \mathsf{R}^{ji} \text{ with } \lambda_j = \frac{n_{\text{tot}}}{\sum_{i=1}^{k} \mathsf{R}^{ji}}.$$

R^{ij} is the cofactor corresponding to element R_{ij} and is a composite measure of transition rates between states such that the initial state is not i. λ_i is a coefficient in units $\mathrm{s\,cm^{-3}}$ that constrains all transition rates so that all particles have made a transition to attain equilibrum. The λ_i are found using the definition of statistical equilibrium. Since $\mathsf{R}^{ij} = \mathsf{R}^{ji}$, the rate equations are linearly dependent, and consequently $\det \mathsf{R} = 0$. Also, the total number of transitions out of any state is equal to the total number of transitions into that state, and thus the sum all elements within any column of R is zero. These two facts imply that for any row of R, the cofactors of the elements within that row are all identical. Thus, the λ_i are degenerate, and it is convenient to reduce the solution to

$$n_i = \lambda \mathsf{R}^{ii} \text{ with } \lambda = \frac{n_{\mathrm{tot}}}{\sum_{i=1}^{k} \mathsf{R}^{ii}}.$$

With the number density n of the transitioning gas species solved for each of the k energy states, the cooling rate $\Lambda(\nu_{ul})$ is well defined.

6.2 CII cooling

The ground-state electronic structure of singly ionized carbon (CII) is $1s^2 2s^2 2p^1$, and the two lowest energy states comprise the doublet ${}^2P_{\frac{1}{2},\frac{3}{2}}$. Coefficients for the forbidden [CII] fine-structure magnetic dipole transition ${}^2P_{\frac{3}{2}} \rightarrow {}^2P_{\frac{1}{2}}$ are given in Table 6.1. The escape probability is assumed to be 0.5 everywhere in the disk, but a more accurate calculation would follow de Jong et al. (1980). Collisions determine the level populations of CII since the gas density nearly everywhere throughout the

Table 6.1. [CII] transition coefficients

u	l	λ_{ul} (μm) [a]	E_{ul} (K)	A_{ul} (s^{1}) [a]	$\gamma_{ul,\,e}$ $\mathrm{cm}^3\,\mathrm{s}^{-1}$ [b]	$\gamma_{ul,\,\mathrm{H}}$ $\mathrm{cm}^3\,\mathrm{s}^{-1}$ [c]	$\gamma_{ul,\,\mathrm{H_2}}$ $\mathrm{cm}^3\,\mathrm{s}^{-1}$ [d]
$^2P_{\frac{3}{2}}$	$^2P_{\frac{1}{2}}$	157.6790	92	2.29×10^{-6}	$3.8 \times 10^{-7} T^{-0.5}$	$5.8 \times 10^{-10} T^{0.02}$	$3.1 \times 10^{-10} T^{0.1}$

[a] NIST Atomic Spectra Database

[b] Tielens (2005, Table 2.7)

[c] Launay & Roueff (1977)

[d] Flower & Launay (1977)

disk is much greater than the critical density for CII, $\sim 10^3 \mathrm{cm}^{-3}$.

Electrons are the most important collisional partners with CII. To estimate collisional de-excitation rate coefficients for a temperature span typical of protoplanetary disks, $30\,\mathrm{K} \lesssim T_{\mathrm{gas}} \lesssim 3000\,\mathrm{K}$, c.f. Figure 2.4, a temperature power law for the $\mathrm{CII} - e^-$ collisional de-excitation coefficient was estimated. Following Osterbrock & Ferland (2006, § 3.5) and with the upper and lower energy states denoted by u and l respectively, the collisional de-excitation rate coefficient γ_{ul} is the product of the de-excitation collisional cross-section σ_{ul} and velocity distribution $f(v)$ integrated over all velocity ranges $v + \mathrm{d}v$ of the colliding partner species e^-,

$$\gamma_{ul} = \int_0^\infty \sigma_{ul} f(v) v \,\mathrm{d}v.$$

In terms of the collision strength $\Omega(u, l)$, the de-excitation collisional cross-section of the gas species with the electron is

$$\sigma_{ul}(v_u) = \frac{\pi\hbar^2}{m_e^2 v_u^2}\frac{\Omega(u,l)}{g_u},$$

where v is the velocity of the gas species, g is the statistical weight of the energy level, m_e is the electron mass, and $\hbar$ is Planck's constant divided by 2π. With the velocity-averaged collision strength as

$$\Upsilon(u,l) = \int_0^\infty \Omega(u,l;E)\exp\left(-\frac{E}{kT_x}\right)\,\mathrm{d}\left(\frac{E}{kT_x}\right),\ E = \frac{1}{2}m_x v_u^2,$$

the de-excitation rate coefficient becomes

$$\begin{aligned}\gamma_{ul} &= \frac{2\pi}{kT_x}^{1/2}\frac{\hbar^2}{m_e^{3/2}}\frac{\Upsilon(u,l)}{g_u}\\ &= \frac{8.629\times10^{-6}}{T_x^{1/2}}\frac{\Upsilon(u,l)}{g_u}.\end{aligned}$$

Properties of the gas species being de-excited, here CII, are denoted with x, T is temperature, and k is the Boltzmann constant. Using collision strengths from Blum & Pradhan (1992), the estimated collisional de-excitation rate disagreed with that of Tielens (2005, Table 2.7) by an order of magnitude. The temperature power law from Tielens (2005) is used instead.

At most, CII cooling constitutes ∼10% of the local gas cooling where water has frozen out of the gas, Figure 6.10. In the settled case, the sudden drop in [CII]

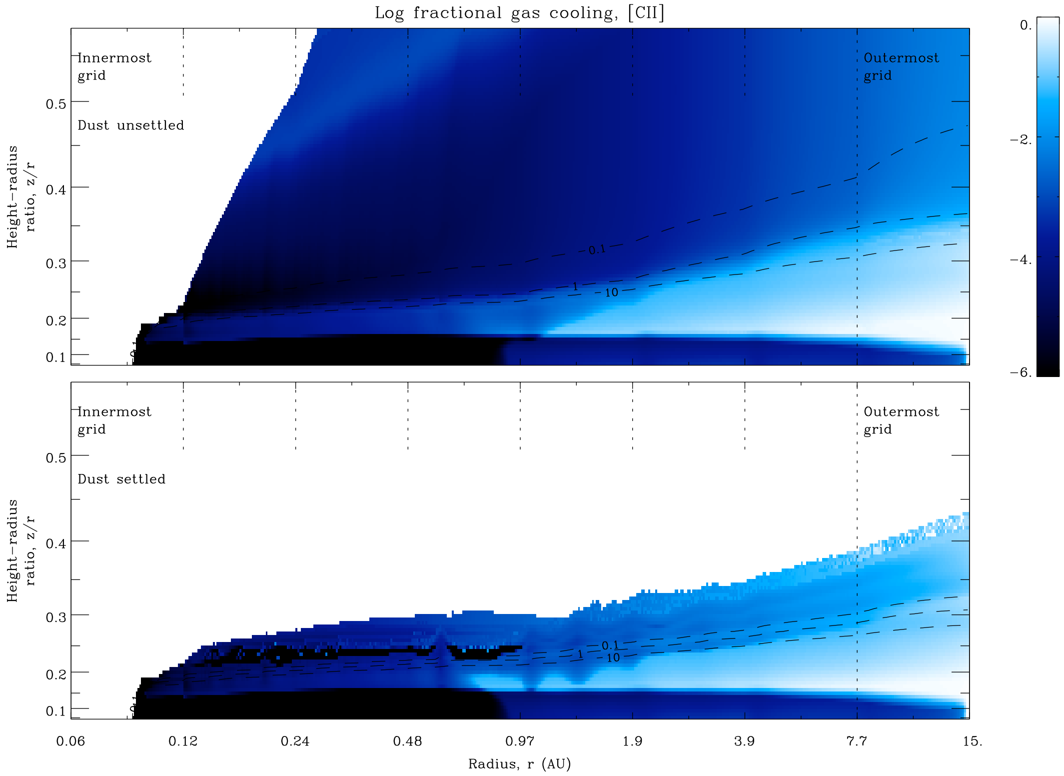

Figure 6.10 The $\log_{10}$ fractional gas cooling due to [CII] emission at $\sim$157 μm for an unsettled disk and a settled disk is plotted as in Figure 6.4. [CII] emission is stronger from a disk with settled dust, however most [CII] emission will originate from beyond the inner disk that is modeled by Pisco.

emission parallel to the disk photosphere corresponds to the sudden cold regime of the temperature inversion in Figure 2.4. From Pisco, [CII] emission is stronger from settled disks compared to unsettled disks, however the majority of [CII] emission will originate from beyond the inner disk that is modeled by Pisco. [CII] at $\sim$157 μm has not yet been detected from protoplanetary disks, but it is expected (Mathews et al., 2010).

Table 6.2. [OI] transition coefficients

u	l	λ_{ul} (μm) [a]	E_{ul} (K)	A_{ul} (s^1) [a]	$\gamma_{ul,\,p}$ cm^3 s^{-1} [b]	$\gamma_{ul,\,\mathrm{H,H_2}}$ cm^3 s^{-1} [c]
$^2P_0$	$^2P_1$	145.5350	98	1.75×10^{-5}	5.0×10^{-9}	$1.5 \times 10^{-10} T^{0.44}$
$^2P_0$	$^2P_2$	44.0573	326	1.34×10^{-10}	1.4×10^{-8}	$1.1 \times 10^{-12} T^{0.8}$
$^2P_1$	$^2P_2$	63.1852	228	8.91×10^{-5}	1.4×10^{-8}	$4.2 \times 10^{-12} T^{0.67}$

[a] NIST Atomic Spectra Database

[b] (Tielens, 2005, Table 2.7)

[c] Collisional rate coefficients for H from Launay & Roueff (1977). Coefficients for H_2 assumed equal to those of H, (Tielens & Hollenbach, 1985)

6.3 OI cooling

The ground-state electronic structure of neutral oxygen (OI) is $1s^2 2s^2 2p^4$, and the three lowest energy states comprise the triplet $^2P_{2,1,0}$. Coefficients for the forbidden [OI] fine-structure magnetic dipole transitions $^2P_0 \rightarrow {}^2P_1$ and $^2P_1 \rightarrow {}^2P_2$ and electric quadrapole transition $^2P_0 \rightarrow {}^2P_2$ are given in Table 6.2. The escape probability is assumed to be 0.5 for all transitions. The $^2P_1 \rightarrow {}^2P_2$ transition is likely to be optically thick due to the high A coefficient, which is not accounted for. A more accurate calculation would follow de Jong et al. (1980). Collisions determine the level populations of OI since the gas density nearly everywhere throughout the disk is much greater than the critical density for the [OI] transitions, $\lesssim 10^4 \mathrm{cm}^{-3}$.

[OI] dominates the gas cooling where water is frozen out of the gas, Figure 6.11. In the settled case and as with [CII], the sudden drop in [OI] emission parallel to the disk photosphere corresponds to the sudden cold regime of the temperature in-

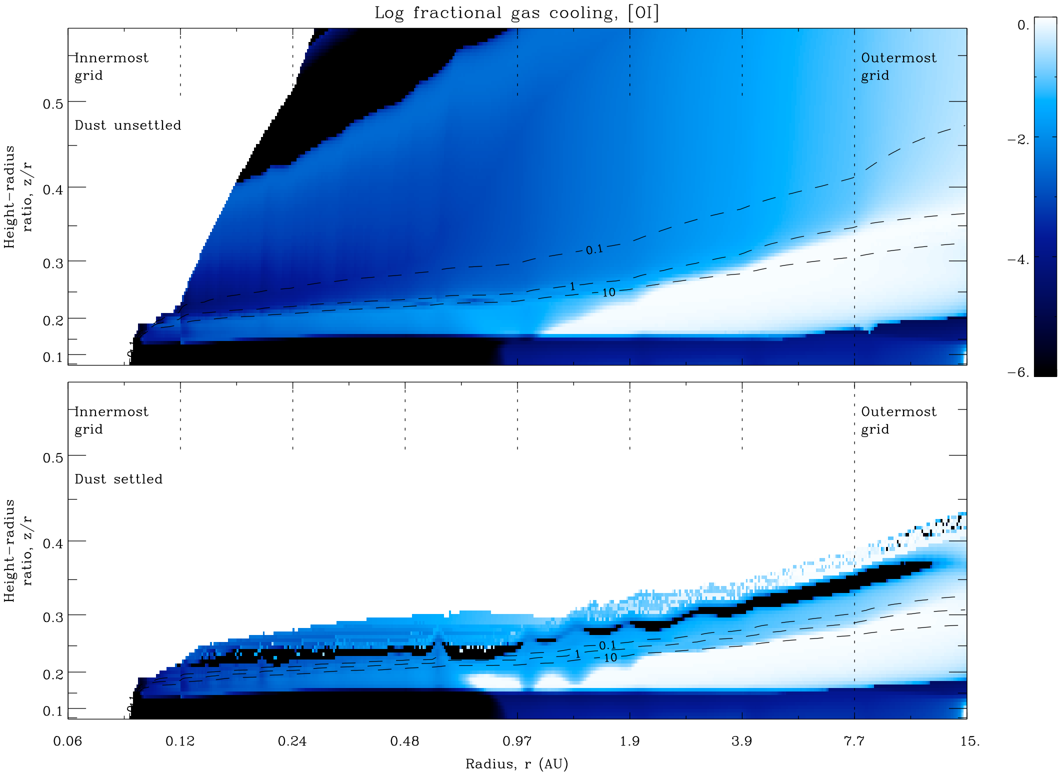

Figure 6.11 The $\log_{10}$ fractional gas cooling due to [OI] emission at $\sim$44, 63, 145 μm for an unsettled disk and a settled disk is plotted as in Figure 6.4. There is little change in the total amount of emission from [OI] comparing unsettled and settled disks.

version in Figure 2.4. Between cases of unsettled and settled dust, the total [OI] emission is comparable. As with [CII], the majority of [OI] emission will originate from beyond the inner disk that is modeled by Pisco. The 63 μm transition has been detected from protoplanetary disks (Mathews et al., 2010), but the transitions at 145 μm and certainly at 44 μm have not yet been observed from disks.

Chapter 7

Conclusion

The computational code Pisco for modeling protoplanetary disks is currently under development and testing. The following modifications discussed in this thesis will yield significant improvements to Pisco's results:

- Temperature should be calculated throughout the disk by balancing heating and cooling processes despite low gas density and/or the sublimation of dust. This provides a check for consistency of heating and cooling calculations interior to inner rim and above the disk photosphere.

- Inconsistencies in radiative transfer by ray tracing across grid boundaries should be corrected to avoid a jagged disk structure and excess ultraviolet radiation deep within the disk. The layout of computational grid cells may need to be changed so that cells increase incrementally in size with radius.

- Chemical abundances should be estimated from chemical models. Assuming a constant abundance throughout the disk will overestimate cooling due to molecular emission, especially above the disk photosphere.

- As a diagnostic, line-of-sight optical depth contours are useful for determining the influence of stellar radiation on the disk and which parts of the disk are observable. Additional contours for lines-of-sight from the star into the disk for wavelengths from X-ray to near-infrared will show the disk depth to which stellar radiation can penetrate. Additional contours for lines-of-sight from an observer into the disk face-on for wavelengths from visible to sub-millimeter will show the depth from which radiation can escape.

While Pisco's calculations are being improved, the code's utility and potential for calculating the physical conditions of the inner disk have already been demonstrated through the following confirmations:

- A disk with settled dust is not "flat," or wedge-shaped, but is flared. An unsettled disk is even more flared than a settled disk.

- Gas and dust temperatures are highly coupled by frequent collisions between gas and dust particles below the disk photosphere. Gas-dust coupling at the disk photosphere is weak but non-negligible. Gas and dust temperatures are decoupled above the disk photosphere.

- The photoelectric effect heats gas to high temperatures where all of the following hold true: ultraviolet light can penetrate, dust exists, and gas-dust coupling is weak to none. The photospheres of both unsettled and settled disks contain hot gas within them, but the gas above the photosphere of an unsettled disk is hotter than that of a settled disk.
- Due to the lack of photoelectric heating above the disk photosphere when the disk is settled, settled disks have a stronger temperature inversion at the disk photosphere than unsettled disks.

With emphasis on the photosphere of the inner disk, Pisco is well positioned to examine the physics that underlies spectroscopic observations of protoplanetary disks. Pisco is poised to test many aspects of disk physics:

- What is the disk profile at the inner rim and at the inner disk surface, and how is the disk profile affected by the settling of dust?
- What are the physical conditions of the gas within the inner disk and at the disk photosphere?
- What kind of heating and cooling processes govern the disk temperature and where do they dominate?
- How do abundances calculated by chemical models compare to observed emission from coolants?

- What does the strength of spectral bands from a molecular species, e.g. HCN, indicate about the physical conditions within the disk?

With the inclusion of NLTE radiative transfer and calculations of level populations for molecular species such as HCN, these questions will be addressed through Pisco's protoplanetary disk model.

This work was funded by NSF grant AST-0607312 and the NSF Graduate Research Fellowship Program.

Bibliography

Armitage, P. J. 2011, Annual Review of Astronomy and Astrophysics, 49, 195

Bitner, M. A., et al. 2008, The Astrophysical Journal, 688, 1326

Blum, R. D., & Pradhan, A. K. 1992, The Astrophysical Journal Supplement Series, 80, 425

Carmona, A., van den Ancker, M. E., Henning, T., Goto, M., Fedele, D., & Stecklum, B. 2008, Astronomy and Astrophysics, 478, 795

Carr, J. S., & Najita, J. R. 2008, Science, 319, 1504

Chiang, E. I., & Goldreich, P. 1997, The Astrophysical Journal, 490, 368

de Jong, T., Dalgarno, A., & Boland, W. 1980, in , 177

Dullemond, C., Hollenbach, D., Kamp, I., & D'Alessio, P. 2007, in Protostars and Planets V, ed. B. Reipurth, D. Jewitt, & K. Keil (University of Arizona Press), 555–572

Dullemond, C. P., & Dominik, C. 2004, Astronomy and Astrophysics, 421, 1075

Dullemond, C. P., & Monnier, J. D. 2010, Annual Review of Astronomy and Astrophysics, 48, 205

Flower, D. R., & Launay, J. M. 1977, Journal of Physics B Atomic Molecular Physics, 10, 3673

Glassgold, A. E., Najita, J., & Igea, J. 2004, The Astrophysical Journal, 615, 972

Gorti, U., & Hollenbach, D. 2008, The Astrophysical Journal, 683, 287

Gorti, U., Hollenbach, D., Najita, J., & Pascucci, I. 2011, The Astrophysical Journal, 735, 90

Haisch, K. E., Lada, E. A., & Lada, C. J. 2001, The Astrophysical Journal Letters, 553, L153

Hartmann, L., Calvet, N., Gullbring, E., & D'Alessio, P. 1998, The Astrophysical Journal, 495, 385

Kamp, I., & Dullemond, C. P. 2004, The Astrophysical Journal, 615, 991

Kenyon, S. J., & Hartmann, L. 1987, The Astrophysical Journal, 323, 714

—. 1995, The Astrophysical Journal Supplement Series, 101, 117

Launay, J. M., & Roueff, E. 1977, Astronomy and Astrophysics, 56, 289

Mathews, G. S., et al. 2010, Astronomy and Astrophysics, 518, L127

Meijerink, R., Poelman, D. R., Spaans, M., Tielens, A. G. G. M., & Glassgold, A. E. 2008, The Astrophysical Journal, 689, L57

Neufeld, D. A., & Kaufman, M. J. 1993, The Astrophysical Journal, 418, 263

Osterbrock, D. E., & Ferland, G. J. 2006, Astrophysics of gaseous nebulae and active galactic nuclei

Pinte, C., Harries, T. J., Min, M., Watson, A. M., Dullemond, C. P., Woitke, P., Mnard, F., & Durn-Rojas, M. C. 2009, Astronomy and Astrophysics, 498, 967

Pontoppidan, K. M., Blake, G. A., van Dishoeck, E. F., Smette, A., Ireland, M. J., & Brown, J. 2008, The Astrophysical Journal, 684, 1323

Pontoppidan, K. M., Salyk, C., Blake, G. A., & Kufl, H. U. 2010, The Astrophysical Journal Letters, 722, L173

Rosseland, S. 1926, The Astrophysical Journal, 63, 218

—. 1936, Theoretical astrophysics ..., Vol. 65

Salyk, C., Pontoppidan, K. M., Blake, G. A., Lahuis, F., van Dishoeck, E. F., & Evans, N. J. 2008, The Astrophysical Journal, 676, L49

Tielens, A. G. G. M. 2005, The Physics and Chemistry of the Interstellar Medium

Tielens, A. G. G. M., & Hollenbach, D. 1985, The Astrophysical Journal, 291, 722

Weingartner, J. C., & Draine, B. T. 2001, The Astrophysical Journal, 548, 296

White, O. R. 1961, The Astrophysical Journal, 134, 85

Williams, J. P., & Cieza, L. A. 2011, Annual Review of Astronomy and Astrophysics, 49, 67

Woitke, P., Kamp, I., & Thi, W. 2009, Astronomy and Astrophysics, 501, 383